Correspondence to:
T. J. Bralower,
bralower@psu.edu

The Habitat of the Nascent Chicxulub Crater

T. J. Bralower[1], J. Cosmidis[1], M. S. Fantle[1], C. M. Lowery[2], B. H. Passey[3], S. P. S. Gulick[2], J. V. Morgan[4], V. Vajda[5], M. T. Whalen[6], A. Wittmann[7], N. Artemieva[8], K. Farley[9], S. Goderis[10], E. Hajek[1], P. J. Heaney[1], D. A. Kring[11], S. L. Lyons[1], C. Rasmussen[2], E. Sibert[12], F. J. Rodríguez Tovar[13], G. Turner-Walker[14], J. C. Zachos[15], J. Carte[1], S. A. Chen[1], C. Cockell[16], M. Coolen[17], K. H. Freeman[1], J. Garber[1], M. Gonzalez[1], J. L. Gray[18], K. Grice[17], H. L. Jones[1], B. Schaefer[17], J. Smit[19], and S. M. Tikoo[20]

[1]Department of Geosciences, Pennsylvania State University, University Park, PA, USA, [2]Institute for Geophysics, Jackson School of Geosciences, University of Texas at Austin, Austin, TX, USA, [3]Department of Earth and Environmental Sciences, University of Michigan, Ann Arbor, MI, USA, [4]Department of Earth Science and Engineering, Imperial College London, London, UK, [5]Department of Palaeobiology, Swedish Museum of Natural History, Stockholm, Sweden, [6]Geophysical Institute, University of Alaska Fairbanks, Fairbanks, AK, USA, [7]Eyring Materials Center, Arizona State University, Tempe, AZ, USA, [8]Planetary Science Institute, Tucson, AZ, USA, [9]Division of Geological and Planetary Sciences, California Institute of Technology, Pasadena, CA, USA, [10]Department of Chemistry, Vrije Universiteit Brussel, Brussels, Belgium, [11]Lunar and Planetary Institute, Houston, TX, USA, [12]Department of Earth and Planetary Sciences, Yale University, New Haven, CT, USA, [13]Departamento de Estratigrafía y Paleontología, Facultad de Ciencias, Universidad de Granada, Granada, Spain, [14]Graduate School of Cultural Heritage Conservation, National Yunlin University of Science and Technology, Yunlin, Taiwan, [15]Earth and Planetary Sciences, University of California, Santa Cruz, CA, USA, [16]School of Physics and Astronomy, University of Edinburgh, Edinburgh, UK, [17]Organic and Isotope Geochemistry Centre, The Institute for Geoscience Research, School of Earth and Planetary Science, Curtin University, Perth, Western Australia, Australia, [18]Materials Research Institute, Pennsylvania State University, University Park, PA, USA, [19]Department of Geology and Geochemistry, VU Universiteit Amsterdam, Amsterdam, The Netherlands, [20]Department of Geophysics, Stanford University, Stanford, CA, USA

Abstract An expanded sedimentary section provides an opportunity to elucidate conditions in the nascent Chicxulub crater during the hours to millennia after the Cretaceous-Paleogene (K-Pg) boundary impact. The sediments were deposited by tsunami followed by seiche waves as energy in the crater declined, culminating in a thin hemipelagic marlstone unit that contains atmospheric fallout. Seiche deposits are predominantly composed of calcite formed by decarbonation of the target limestone during impact followed by carbonation in the water column. Temperatures recorded by clumped isotopes of these carbonates are in excess of 70°C, with heat likely derived from the central impact melt pool. Yet, despite the turbidity and heat, waters within the nascent crater basin soon became a viable habitat for a remarkably diverse cross section of the food chain. The earliest seiche layers deposited with days or weeks of the impact contain earliest Danian nannoplankton and dinocyst survivors. The hemipelagic marlstone representing the subsequent years to a few millennia contains a nearly monogeneric calcareous dinoflagellate resting cyst assemblage suggesting deteriorating environmental conditions, with one interpretation involving low light levels in the impact aftermath. At the same horizon, microbial fossils indicate a thriving bacterial community and unique phosphatic fossils including appendages of pelagic crustaceans, coprolites and bacteria-tunneled fish bone, suggesting that this rapid recovery of the base of the food chain may have supported the survival of larger, higher trophic-level organisms. The extraordinarily diverse fossil assemblage indicates that the crater was a unique habitat in the immediate impact aftermath, possibly as a result of heat and nutrients supplied by hydrothermal activity.

Plain Language Summary The newly formed Chicxulub crater was rapidly filled by seawater then disturbed by tsunami and seiche waves. Sedimentary layers deposited as wave energy declined provide a unique window into the environment of the nascent crater in the months and years to millennia after the impact. Geochemical data show temperatures in hotter regions of the crater in excess of 70°C for the first few years with heat derived from the underlying melt sheet via hydrothermal circulation. Cooler regions of the crater became habitats soon after impact with a suite of fossils indicating diverse life on the seafloor and sea surface, ranging from microbes to marine arthropods, and possibly fish. We suggest that this community was sustained by nutrients and heat from the hydrothermal system. The rapid early

Author Contributions:

Conceptualization: T. J. Bralower
Data curation: T. J. Bralower
Formal analysis: T. J. Bralower, J. Cosmidis, M. S. Fantle, C. M. Lowery, B. H. Passey, J. V. Morgan, V. Vajda, A. Wittmann, N. Artemieva, K. Farley, E. Hajek, P. J. Heaney, S. L. Lyons, C. Rasmussen, E. Sibert, F. J. Rodríguez Tovar, G. Turner-Walker, J. C. Zachos, J. Carte, S. A. Chen, M. Coolen, K. H. Freeman, J. Garber, M. Gonzalez, J. Smit
Funding acquisition: T. J. Bralower, S. P. S. Gulick, J. V. Morgan, V. Vajda, S. Goderis, D. A. Kring, C. Cockell, K. H. Freeman
Investigation: T. J. Bralower, J. Cosmidis, M. S. Fantle, B. H. Passey, S. P. S. Gulick, J. V. Morgan, V. Vajda, M. T. Whalen, A. Wittmann, N. Artemieva, K. Farley, S. L. Lyons, C. Rasmussen, E. Sibert, F. J. Rodríguez Tovar, G. Turner-Walker, J. L. Gray, S. M. Tikoo
Methodology: T. J. Bralower, M. S. Fantle, J. L. Gray, S. M. Tikoo
Project administration: T. J. Bralower
Resources: T. J. Bralower
Writing - original draft: T. J. Bralower, J. Cosmidis, M. S. Fantle, B. H. Passey, V. Vajda, K. Farley, C. Rasmussen, F. J. Rodríguez Tovar
Writing – review & editing: T. J. Bralower, J. Cosmidis, M. S. Fantle, C. M. Lowery, S. P. S. Gulick, J. V. Morgan, M. T. Whalen, A. Wittmann, S. Goderis, E. Hajek, P. J. Heaney, D. A. Kring, S. L. Lyons, C. Rasmussen, E. Sibert, F. J. Rodríguez Tovar, G. Turner-Walker, J. C. Zachos, J. Carte, C. Cockell, M. Gonzalez, B. Schaefer, J. Smit, S. M. Tikoo

recovery in the Chicxulub crater and ocean above demonstrates the resiliency of life under extraordinarily harsh conditions, which has important ramifications for early life on Earth and life on other planets.

1. Introduction

In one of the most rapid geomorphic events in Earth history, the 200-km diameter Chicxulub crater formed in minutes to hours (Morgan et al., 2016) and caused major environmental upheaval that led to mass extinction marked by the Cretaceous-Paleogene (K-Pg) boundary (Hildebrand et al., 1991; Kring & Boynton, 1992; Schulte et al., 2010). The shallow sea as well as the carbonate and evaporite rocks at the location of impact (i.e., the target rocks), amplified the environmental effects of the event. Prolonged impact winter, cessation of photosynthesis, and perhaps acid rain resulting from release of SO_2 from evaporite sulfates (Alvarez et al., 1980; Artemieva & Morgan, 2017; Brugger et al., 2017; Gulick et al., 2019; Kring, 2007; Prinn & Fegley, 1987; Tabor et al., 2020; Toon et al., 1982; Vellekoop et al., 2014) were likely major killing mechanisms on land and in the oceans. These effects may have been enhanced by soot released by wildfires (Tschudy et al., 1984; Wolbach et al., 1990) and combusted target rock hydrocarbons (Kaiho et al., 2016; Lyons et al., 2020), and carbonate dust (Artemieva & Morgan, 2020), though this latter material has not been identified in boundary deposits. The impact occurred either between eruptive phases of the Deccan traps (Schoene et al., 2019), or largely before these phases (Sprain et al., 2019). CO_2-related warming from these eruptions was either over (Hull et al., 2020) or served as a minor mitigating factor (Chiarenza et al., 2020). The effects of the impact are, however, directly tied to the mass extinction event (Artemieva & Morgan, 2017, 2020; Gulick et al., 2019; Schulte et al., 2010). Once formed, impact craters such as Chicxulub can provide unique habitats for life (Cockell et al., 2003; Russell & Hall, 2006), a function that may also have been in operation early in Earth history (Russell & Hall, 2006). Hydrothermal systems initiated by impact have the potential to release nutrients and energy for microbial activity (Abramov & Kring, 2007; Newsom et al., 2001; Osinski et al., 2013; Rathbun & Squyres, 2002), and the presence of hydrothermal minerals within the crater's peak ring confirm that hot fluids circulated in these rocks after crater formation (Kring et al., 2020). These impact lithologies today host diverse microbial communities shaped by the impact event (Cockell et al., 2019). However, to this point there has been little exploration of the connection between hydrothermal activity and local marine life in the aftermath of an impact (Kring et al., 2020; O'Sullivan et al., 2016).

The geological record of the Chicxulub crater offers clues regarding the dynamic processes that occurred in the immediate aftermath of the impact and affected the habitability of the nascent crater. Immediately after impact, an ~200-km-wide impact basin was formed with an internal 80- to 90-km diameter topographic peak ring surrounding a central basin containing a thick suevite (i.e., melt-bearing impact breccia) layer above an impact melt sheet (Abramov & Kring, 2007). Heterogeneity in topography, structure, and nature of the near-surface rocks led to considerable variability in heat and fluid flow, which would have affected the chemistry of the initial waters that entered the crater. While Chicxulub has been the target of extensive geophysical exploration in the past (Gulick et al., 2013; Morgan & Warner, 1999), existing boreholes were either only spot cored or located on the inner ring crater slope where accommodation space was limited and the boundary sequence is condensed and incomplete (Arz et al., 2004; Goto et al., 2004). The Yaxcopoil-1 (YAX-1) core, drilled adjacent to the inner ring of the crater contains evidence for hydrothermal circulation in impact breccias (Hecht et al., 2004; Lüders & Rickers, 2004; Zürcher & Kring, 2004) and overlying Paleogene limestones that suggests that hydrothermal activity persisted for hundreds of thousands of years after the impact (Rowe et al., 2004). However, repeated mass wasting events at YAX-1 from the adjacent inner crater rim obscure the sedimentary record of the years after the impact (Wang et al., 2013; Whalen et al., 2013), limiting our ability to document the history of the recovery of life and of hydrothermal activity.

International Ocean Discovery Program-International Continental Scientific Drilling Program (IODP-ICDP) Expedition 364 drilled into the Chicxulub peak ring at Site M0077 (Morgan & Gulick, 2018). The site was located in a depression on top of the peak ring, providing the accommodation space for the accumulation of a remarkable boundary sequence. Site M0077 recovered 587 m of felsic basement rocks overlain by 130 m of suevite. The lowermost suevite was emplaced as the central uplift collapsed to form the peak ring, and suevite deposition continued during ocean resurge, seiche (internal to the crater) and tsunami waves
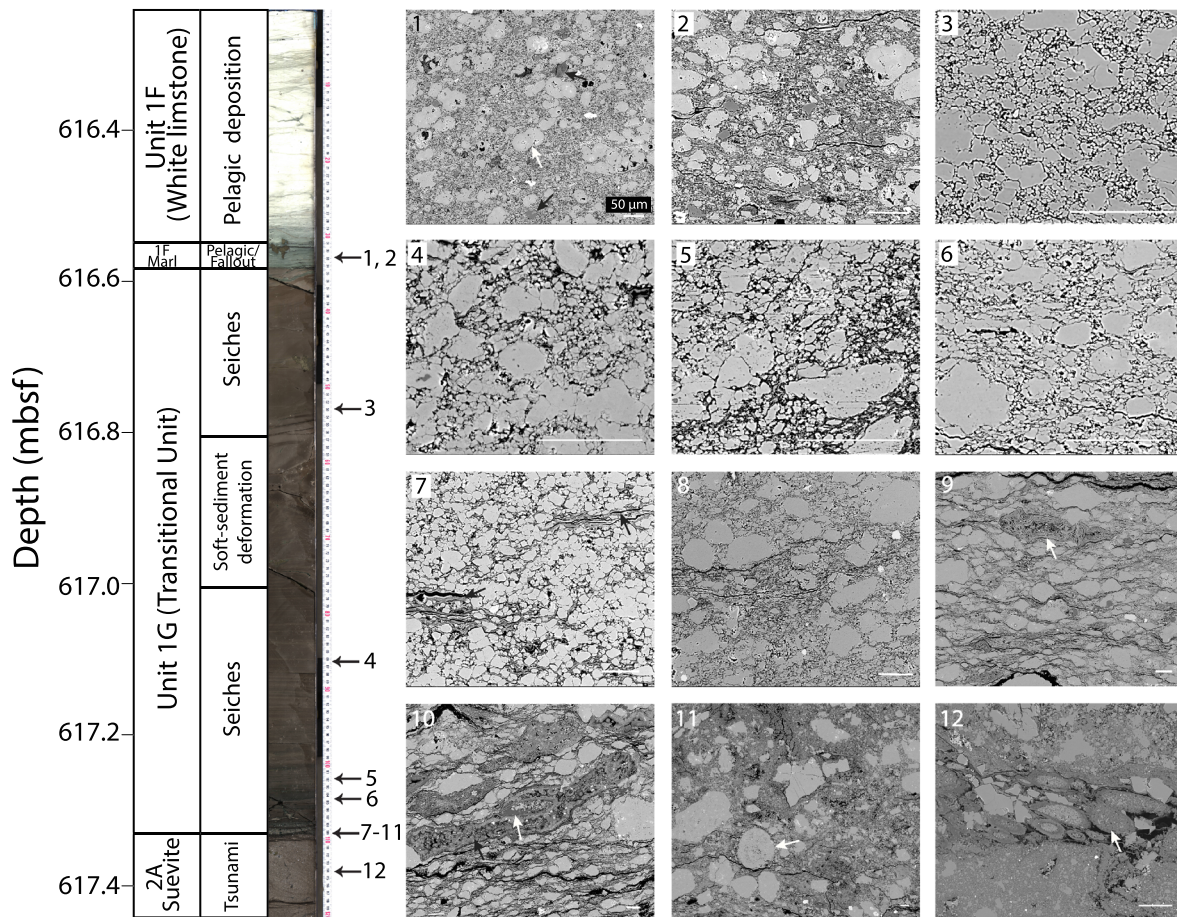
Figure 1. Photograph of the uppermost suevite (Unit 2A), transitional unit (Unit 1G) and green marlstone, and Danian pelagic limestone (Unit 1F) (units after Gulick et al., 2017) in Core 40R-1, and backscatter (BSE) images showing origin of micrite (core photo shows the location of samples). Depositional environment after Gulick et al. (2019) and Whalen et al. (2018). Pl. 1, 2. Foraminiferal calcite (white arrow) with a small amount of silicate melt (black arrows), 32–34 cm (616.56–616.58 mbsf); Pl. 3–7 Micrite derived from decarbonation-carbonation (more angular grains); black arrows in Pl. 7 are clay; Pl. 3. 50–55 cm (616.74–616.79 mbsf), Pl. 4. 84–89 cm (617.08–617.13 mbsf), Pl. 5. 100–104 cm (617.24–617.28 mbsf), Pl. 6. 104–105 cm (617.28–617.29 mbsf); Pl. 8–12. Micrite largely derived from melt (rounded grain shown with white arrow in Pl. 11) along with silicate melt (white arrows in Pl. 9, 10), altered silicate melt (black arrow in Pl. 10), and mixed carbonate-silicate ash (white arrow in Pl. 12); Pl. 7–11. 108–110 cm (617.32–617.34 mbsf), Pl. 12. 110–118 cm (617.34–617.42 mbsf). Scale bars 50 μm.

(Gulick et al., 2019). Site M0077 granitoid rocks and suevites show mineralogical and paleomagnetic evidence of long-lasting hydrothermal circulation (Kring et al., 2020; Morgan & Gulick, 2018). The uppermost 8.5 m (617.33–625.85 m below sea floor, mbsf) of these deposits, largely very fine grained, layered suevite that was laid down by a succession of seiches, are capped by a coarser grained, cross-bedded tsunami-deposited unit. The suevite (Unit 2A of Gulick et al., 2017) grades into a 75 cm generally upward fining, brown, fine-grained limestone termed the "transitional unit" (Lowery et al., 2018) (Unit 1G of Gulick et al., 2017; 617.33 to 616.58 mbsf), which was deposited by settling, tsunami, and seiches (Whalen et al., 2018). This unit is in turn overlain by a 3-cm-thick green marlstone (Gulick et al., 2017); 616.58 to 616.55 mbsf that grades into pelagic white limestone (Unit 1F of Gulick et al. (2017)) (Figure 1). The lower 52 cm of the transitional unit contains mm-scale laminations and graded beds, and the upper 19 cm also contains cross beds and hummocky cross stratification which signify deposition by bottom currents associated with residual seiches within the crater (Whalen et al., 2018). The fine silt and clay grain size of the transitional unit suggests that the majority of sediment was delivered by resuspension and settling. A 20-cm interval of soft-sediment deformation occurs in the middle of the transitional unit, and the upper ~15 cm of the unit is burrowed (Lowery et al., 2018). The transitional unit contains clay and pyrite, and is bounded by two intervals enriched in charcoal, which likely settled from the ocean surface transported by either wave energy or through the atmosphere (Gulick et al., 2019). The

occurrence of charcoal and evidence for high-energy transport suggests that the majority of the transitional unit was deposited very rapidly within days to, at most, years after the impact. This interpretation was originally based on Helium-3 measurements and Stokes Law calculations (Lowery et al., 2018) and is confirmed by enrichment of Ir in the uppermost transitional unit and green marlstone (between 616.60 and 616.55 mbsf) that indicates settling of meteoritic material, likely within a few years of the impact (Goderis et al., 2019). Site M0077 thus represents the most expanded postimpact drill core record yet recovered of the immediate aftermath of the Chicxulub impact event (Gulick et al., 2019).

The transitional unit contains rare calcareous nannofossils and common planktic foraminifera, with survivor species of the latter group becoming more common upsection, indicating the appearance of pelagic life in the crater at least by the time burrows suggest a benthic infauna, less than a few years after impact (Lowery et al., 2018). The majority of the unit is composed of microcrystalline calcite, also known as micrite. Scanning electron microscopy (SEM) reveals rare microcrystals that have been interpreted as microbial in origin (Bralower et al., 2020). The bulk of the micrite was likely derived from CaO via thermal decarbonation (emission of CO_2) of sedimentary target-rocks during impact followed by carbonation (backreaction via addition of CO_2) to $CaCO_3$, as suggested for select carbonate particles found at other K-Pg sites (Bralower et al., 2020; Schulte et al., 2009; Yancey & Guillemette, 2008). However, the mechanics of carbonation are not well understood and it is unclear whether it took place in the late stages of impact plume expansion, during the resurge of ocean waters back into the crater, in the water column after crater flooding, or during burial in the months to years that the transitional unit was formed.

Rapid deposition of the transitional unit offers the potential to determine the effects of reduced photosynthesis, impact winter and hydrothermal activity on life at the dawn of the Cenozoic era. Yet the proxy record can only be evaluated once the formation of micrite is constrained. Moreover, interpretation of the fossil record is complicated by the high-energy depositional environment in which reworking of microscopic plankton tests is common (Lowery et al., 2018). Here we explore the origin of the materials in the transitional unit and green marlstone on top of Chicxulub's peak ring at Site M0077 and probe evidence for recovery of the food chain in the early crater in the first months to thousands of years of the Cenozoic. We use optical microscopy, SEM and transmission electron microscopy (TEM), clumped, strontium, and carbon and oxygen stable isotopes (see supporting information Text S1), and current age models to constrain conditions in the early crater and compare them to the fossil evidence for the recovery of life at ground zero. Our results illustrate that, despite harsh postimpact conditions, the incipient crater became home to the most diverse postimpact marine assemblage documented to date. This illustrates that craters can be viable habitats for life even in the immediate aftermath of impact.

2. Results

2.1. Character of Micrite

Dramatic changes in the size and shape of micrite particles from the upper suevite through the transitional unit into the green marlstone are observed via backscatter electron microscopy (BSE) (Figure 1 and supporting information Figure S1). Abundant micrite is found in the upper suevite (617.54 to 617.43 mbsf) where it is generally angular in shape. In the topmost suevite (617.43 to 617.33 mbsf) and lowermost transitional unit (617.33 to 617.30 mbsf), micrite particles are generally rounded to subrounded, flattened, and 10 to 150 μm in size, and samples have a low porosity and a high clay content, as observed in BSE images (Figure 1; Pl. 7–11; supporting information Figure S1; Pl. 6–10). The compacted nature of rounded micrite particles in this interval (Figure 1; Pl. 8–10; supporting information Figure S1; Pl. 6–9) indicates alteration by pressure solution during burial. In the remainder of the transitional unit, between 617.33 and 616.58 mbsf, micrite particles are generally highly irregular in size, and smaller, between 0.5 and 20 μm, more angular in shape, densely packed but rarely compressed, and with a lower clay content (Figure 1; Pl. 3–6; supporting information Figure S1; Pl. 2–5). Calcite in the green marlstone (616.58 to 616.55 mbsf) is composed of miniscule planktic foraminifera (generally 20 to 40 μm) and very fine micrite (<0.5 to 2 μm; Figure 1; Pl. 1, 2; supporting information Figure S1; Pl. 1). Rare silicate melt particles are also observed (Figure 1; Pl. 1; supporting information Figure S2; Pl. 1–5) and clay content increases in this interval. The fine micrite resembles micrite in the transitional unit under cross-polarized light and is distinct from micrite in the overlying white limestone.
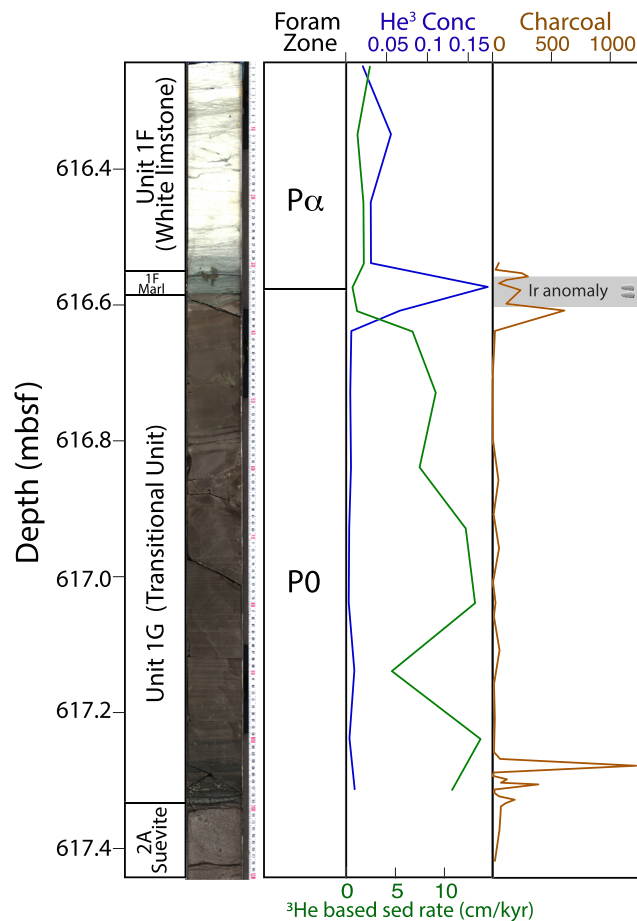
Figure 2. Stratigraphy of uppermost suevite (Unit 2A), transitional unit (Unit 1G), and green marlstone and Danian pelagic limestone (Unit 1F) (units after Gulick et al., 2017) in Core 40R-1. Planktic foraminiferal Zones after Lowery et al. (2018); He isotopes after Lowery et al. (2018) and data herein; counts of charcoal grains after Gulick et al. (2019). Small gray drops indicate occurrence of melt droplets.

2.2. Character of Charcoal and Pyrite

Charcoal is generally rare throughout the transitional unit but is common in two intervals (Figure 2): (1) at the base of the transitional unit and the underlying cross-bedded sand-sized interval at the top of the uppermost suevite (617.34 to 617.27 mbsf) and (2) at the top of the transitional unit, and especially in the overlying green marlstone (616.605 to 616.545 mbsf; Figure 3, Pl. 1, 2). The lowermost transitional unit contains several distinct layers of pyrite (Figure 3; Pl. 6), while the green marlstone contains a diffuse pyritic interval between 616.56 and 616.545 mbsf (Figure 3, Pl. 1, 2) (Gulick et al., 2019) with two thin concentrated layers, as well as several large (centimeter-sized) pyrite nodules (Goderis et al., 2019). A distinct band of pyrite also occurs at 617.24 to 617.25 mbsf. Two other intervals contain abundant pyrite without a corresponding peak in charcoal, a band at 617.0 to 616.99 mbsf (Figure 3, Pl. 5) at the base of the interval of soft sediment deformation, and two lenses at 617.22 to 617.24 mbsf.

Charcoal is high-grade and preserves original wood structure (supporting information Figure S3; Pl. 1–12); petrified wood composed of C, P, and Si as analyzed in Energy Dispersive X-ray Spectrometry (EDS) is also found (Figure 4; Pl. 10–12; supporting information Figure S4; Pl. 10–12). Pyrite in all intervals is preserved as 5- to 100-μm rhombic and hexagonal sheet-like crystals (supporting information Figure S4; Pl. 1), and as 10- to 75-μm-long blades that look like shards at the base of the green marl-stone (Figure 4; Pl. 1, 2; supporting information Figure S4; Pl. 5; supporting information Figure S5; Pl. 7–9). BSE images of hexagonal and blade-like pyrite often show remnant woody structure including grainy texture and pits, even in the intervals where charcoal is rare or absent (Figure 4; Pl. 4–6); images also illustrate grains that preserve a transition between partially and more fully pyritized areas (Figure 4; Pl. 4, 5). BSE images of pyrite grains from the base of the transitional unit show delicate needle clusters that we interpret as pyritized conifer needles (Figure 4; Pl. 7, 8; supporting information Figure S4; Pl. 4). The organic matter of these needles is exposed when damaged by the electron beam (supporting information Figure S4; Pl. 7–9). Both upper and lower transitions contain up to 400-μm unburned woody material, sometimes with delicate organic structures (supporting information Figure S3; Pl. 10, 11).

2.3. He Isotopes

We have measured ^{3}He on two samples from the uppermost transitional unit and combine these data with values from Lowery et al. (2018). Compared to deeper in the transitional unit, measurements at 616.605 and 616.57 mbsf show increasing ^{3}He contents, which suggest slower sedimentation rates (Figure 2; see supporting information Table S2).

2.4. Stable O and C Isotopes

Bulk carbonate δ^{18}O values lie between −6.5‰ and −8.7‰ in the uppermost suevite and lowermost transitional unit (617.42 to 617.31 mbsf), then increase to −6.8‰ to −5.7‰ for most of the transitional unit (617.24 to 616.73 mbsf), then show a steady increase to −2.3‰ just above the green marlstone (616.54 mbsf) (Figure 5). Bulk carbonate δ^{13}C values generally increase through the uppermost suevite and transitional unit (617.47 to 616.73 mbsf) from 0.48‰ to 1.45‰, although an interval of low values also occurs in the interval of soft-sediment deformation, including samples at 616.93 to 616.84 mbsf (Figure 5). Values decrease at the top of the transitional unit and within the lower green marlstone (between 616.73 and 616.57 mbsf) from 1.45‰ to 0.75‰ then increase through the remainder of the green marlstone and the white limestone from 0.75‰ (616.5 mbsf) to 1.44‰ (616.25 mbsf).
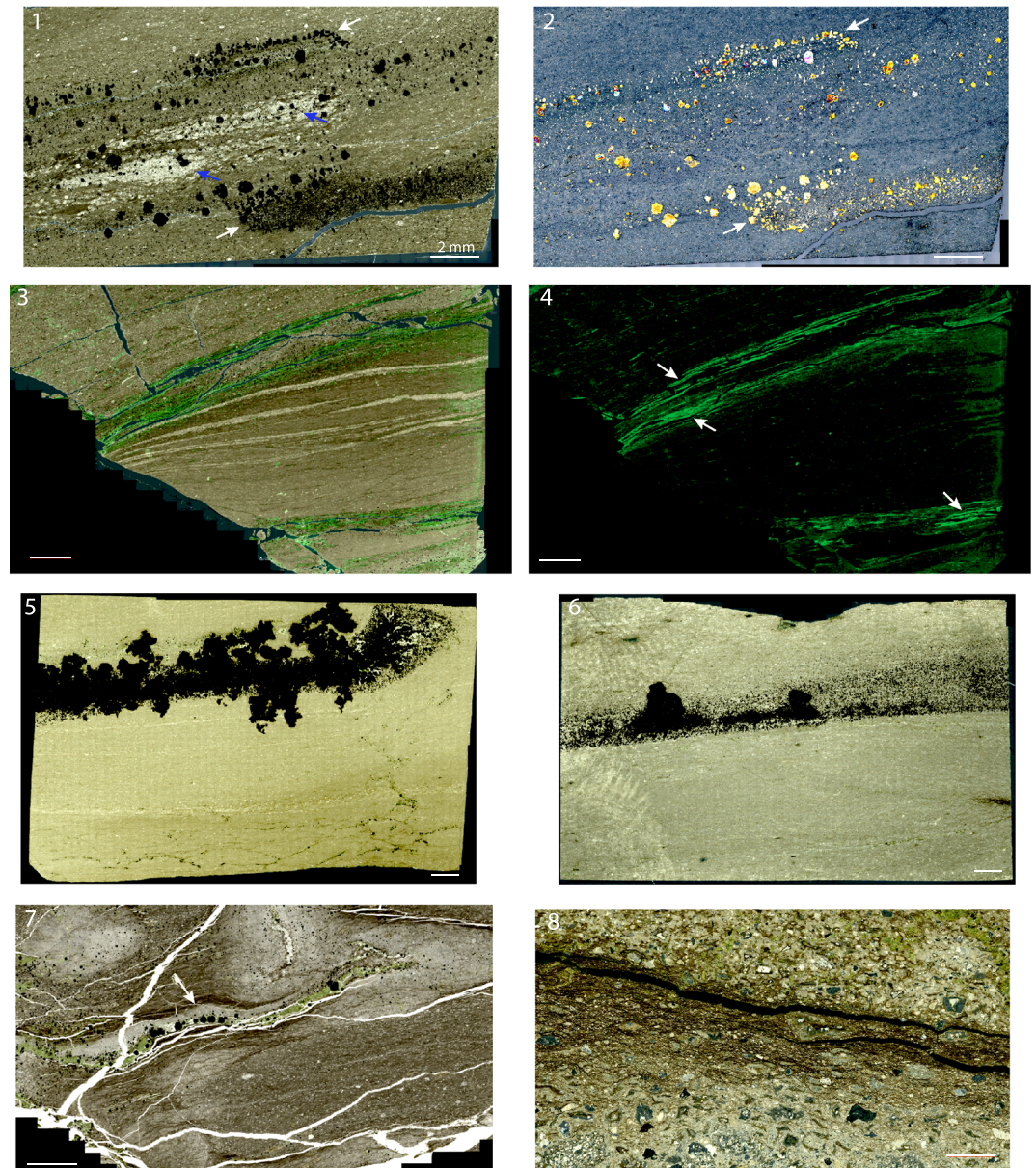
Figure 3. Thin section views of important features in the uppermost suevite, transitional unit and green marlstone. Pl. 1, 2. Upper pyritized charcoal layers in green marlstone. Pl. 1. Cross polarized light (white arrows show apparent bedforms; blue arrows show foraminiferal lags, see Discussion); Pl. 2. Reflected light (white arrows show apparent bedforms; see Discussion). Pl. 3, 4. Boundary between transitional unit and green marlstone showing clay seams and possible algal mats (as shown by green epiflourescence (shown by arrows in Pl. 4, see Discussion)); Pl. 3. Cross-polarized light-Epiflourescence; Pl. 4. Epiflourescence. Pl. 5, 6. Pyrite layers in lower transitional unit cross-polarized light. Pl. 7. Fluid escape structure in lowermost transitional unit with vein (shown with arrow), cross-polarized light. Pl. 8 Alternating interval of melt rich (base and top) and carbonate rich (middle) suevite, cross-polarized light. Samples all in Core 40R-1: Pl. 1, 2. 31–32 cm (616.54–616.56 mbsf); Pl. 3, 4. 33.5–34.5 cm (616.575–616.585 mbsf); Pl. 5. 100–104 cm (617.24–617.28 mbsf); Pl. 6. 104–105 cm (617.28–617.29 mbsf); Pl. 7. 106–108 cm (617.30–617.32 mbsf); Pl. 8. 108–110 cm (617.32–617.34 mbsf). Scale bars represent 2 mm.

2.5. Clumped Isotopes

Clumped isotope-based temperatures are $88 \pm 11°C$ (1σ) for the uppermost suevite (617.47 to 617.34 mbsf), $73 \pm 13°C$ (1σ) for most of the transitional unit (617.31 to 616.64 mbsf) (Figure 5), and decrease within the uppermost transitional unit and green marlstone to $27 \pm 7°C$ in the overlying Danian foraminiferal limestone (616.54 to 616.25 mbsf).
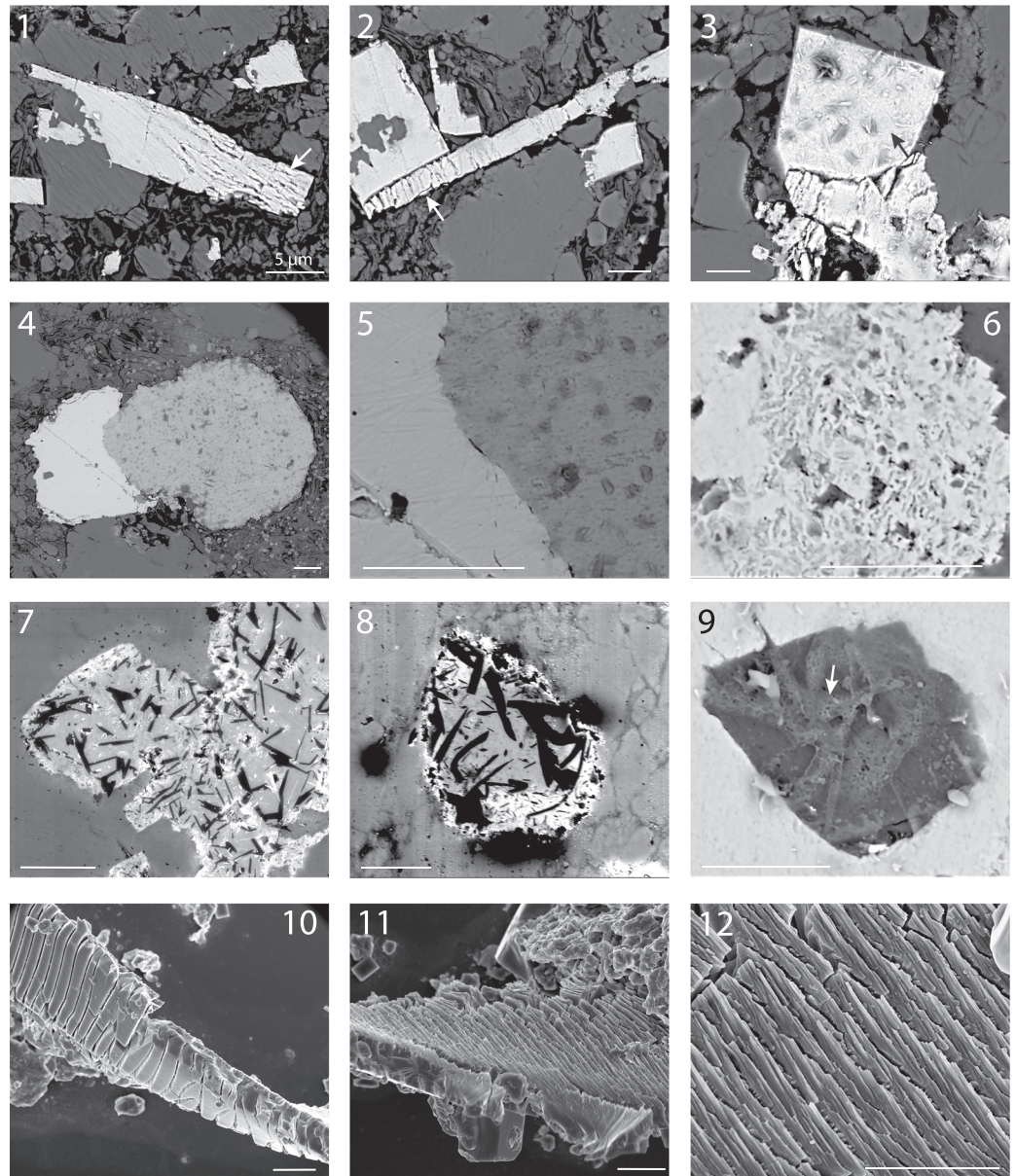
Figure 4. Backscattered electron (BSE) and secondary electron images of pyrite and petrified wood from the lower transitional unit and green marlstone. Pl. 1, 2. Pyrite shards preserving wood structure (arrows); Pl. 3. Pyrite showing wood structure (arrow). Pl. 4, 5. Pyrite showing more (left) and less (right) pyritized areas with wood structure (right); Pl. 5 is close up view of the boundary between the two areas in Pl. 4. Pl. 6. Area of pyrite showing organic structure. Pl. 7, 8. Pyrite containing dark carbon needles (possible conifer needles). Pl. 9. Dolomite (shown by arrow as identified in EDS) underlying pyrite grain. Pl. 10–12. Petrified wood. Samples all in Core 40R-1: Pl. 1, 2. 31–32 cm (616.55–616.56 mbsf); Pl. 3. 100–104 cm (617.24–617.28 mbsf); Pl. 4–6. 32–34 cm (616.56–616.58 mbsf); Pl. 7, 8. 100–104 cm (617.24–617.28 mbsf); Pl. 9. 32–34 cm (616.56–616.58 mbsf); Pl. 10–12. 31 cm (616.55 mbsf). Pl. 1–9. BSE images of thin sections; Pl. 10–12. secondary electron images of strewn slides. Scale bars represent 5 μm.

2.6. Strontium Isotopes and Trace Elements

Strontium isotopic compositions ($^{87}Sr/^{86}Sr$) of sample aliquots leached in 0.1-M ammonium acetate-acetic acid buffer (pH 4.7) and 0.1 N HCl are similar suggesting that Sr is derived from carbonate (see supporting information Figure S6c). There is likewise no correlation between Sr and lithogenic indicators such as Al that suggests an influence of clay dissolution on $^{87}Sr/^{86}Sr$. The $^{87}Sr/^{86}Sr$ ratios of weak HCl-soluble sediment systematically decrease in the lower transitional unit to ~0.70763 in the slump, and then increase to ~0.70771
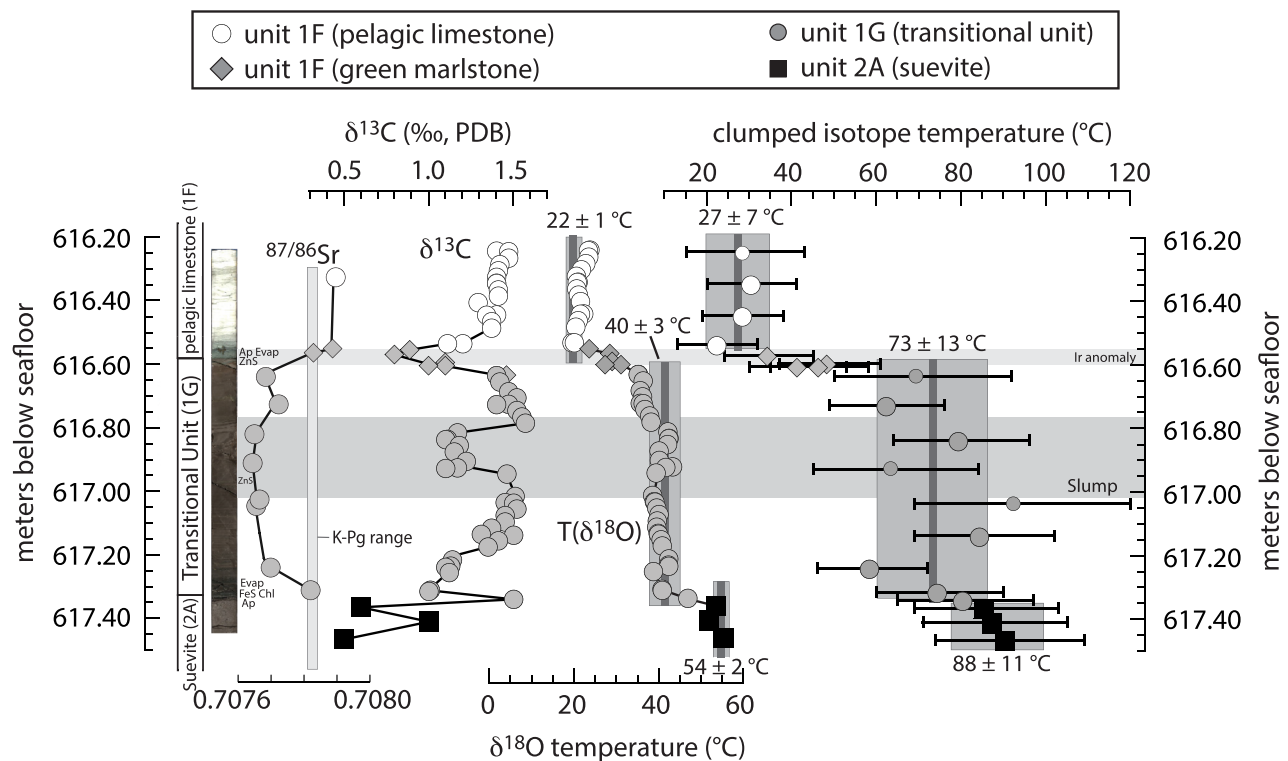
Figure 5. Strontium, carbon, oxygen, and clumped isotope data from the uppermost suevite (Unit 2A), transitional unit (1G), the green marlstone, and pelagic limestone (1F). Interval of soft-sediment deformation is shown by the horizontal gray shaded area as is interval of highest Ir enrichment after Goderis et al. (2019). Sr isotope values are from HCl leaches. The $\delta^{18}O$ temperatures are calculated from $\delta^{18}O_{cc}$ values using the relation of Kim and O'Neil (1997), assuming a seawater $\delta^{18}O$ value of $-1‰$. Clumped isotope temperatures are calculated from Δ_{47} values following Petersen et al. (2019). Error bars for clumped isotopes are 95% confidence intervals, and smaller symbols denote samples that were not analyzed in replicate. Gray vertical bars indicate mean temperature values ($\pm1\sigma$) for the pelagic limestone (1F), the transitional unit (excluding the interval marked tr.), and the uppermost suevite (2A). Range of Sr isotope values for K-Pg sections (Martin & Macdougall, 1991) is shown. Occurrences of hydrothermal ZnS, pyrite, apatite, and evaporite are indicated.

in the upper transitional unit (Figure 5). More radiogenic values (0.70782–0.70789) are recorded in the overlying green marlstone and Danian foraminiferal limestone, values that exceed contemporaneous K-Pg boundary seawater ($\leq$0.707828 ± 0.000004; McArthur & Howarth, 2004).

2.7. Micropaleontology

Samples from the lowermost and uppermost transitional unit and the green marlstone were taken every 0.5 cm for nannoplankton and 2 cm for palynomorphs. Thin sections were also observed in both intervals. Nannoplankton in the lowermost transitional unit include rare specimens of Upper Cretaceous species along with rare specimens of the survivors *Braarudosphaera* spp., *Cyclagelosphaera reinhardtii*, and *Zeugrhabdotus sigmoides* (supporting information Figure S7; Pl. 1–4, 9, 10). A single specimen of the basal Danian marker, *Biantholithus sparsus* is observed at 617.295 mbsf (supporting information Figure S7; Pl. 5, 6). Dinoflagellates in the lower interval (at 617.3 mbsf) are rare but exclusively represented by the cyst *Trithyrodinium evittii* (supporting information Figure S7; Pl. 11, 12). Nannoplankton in the green marlstone (616.58 to 616.545 mbsf) include abundant small fragments of a primitive form of *Cervisiella* spp. (Supporting Information S1 and Figure S7; Pl. 7, 8), but lack the Cretaceous survivor taxa with only very rare reworked specimens of long-ranging Cretaceous species. A single specimen of the earliest Danian genus *Neobiscutum* is observed at 616.575 mbsf (supporting information Figure S8; Pl. 9). There are no organic-walled dinoflagellates in the green marlstone but cyanobacterial fossils are common (Bralower et al., 2020) (supporting information Figure S8; Pl. 1–8). The green marlstone also contains a diverse and abundant assemblage of planktic and benthic foraminifera (the latter represented by at least 63 species typical of the "Velasco Fauna"; Alegret & Thomas, 2001). Earliest Danian planktic foraminifera here include *Parvularugoglobigerina*, *Woodringina*, *Praemurica, Eoglobigerina,* and the Cretaceous survivor, *Guembelitria* (Lowery et al., 2018).
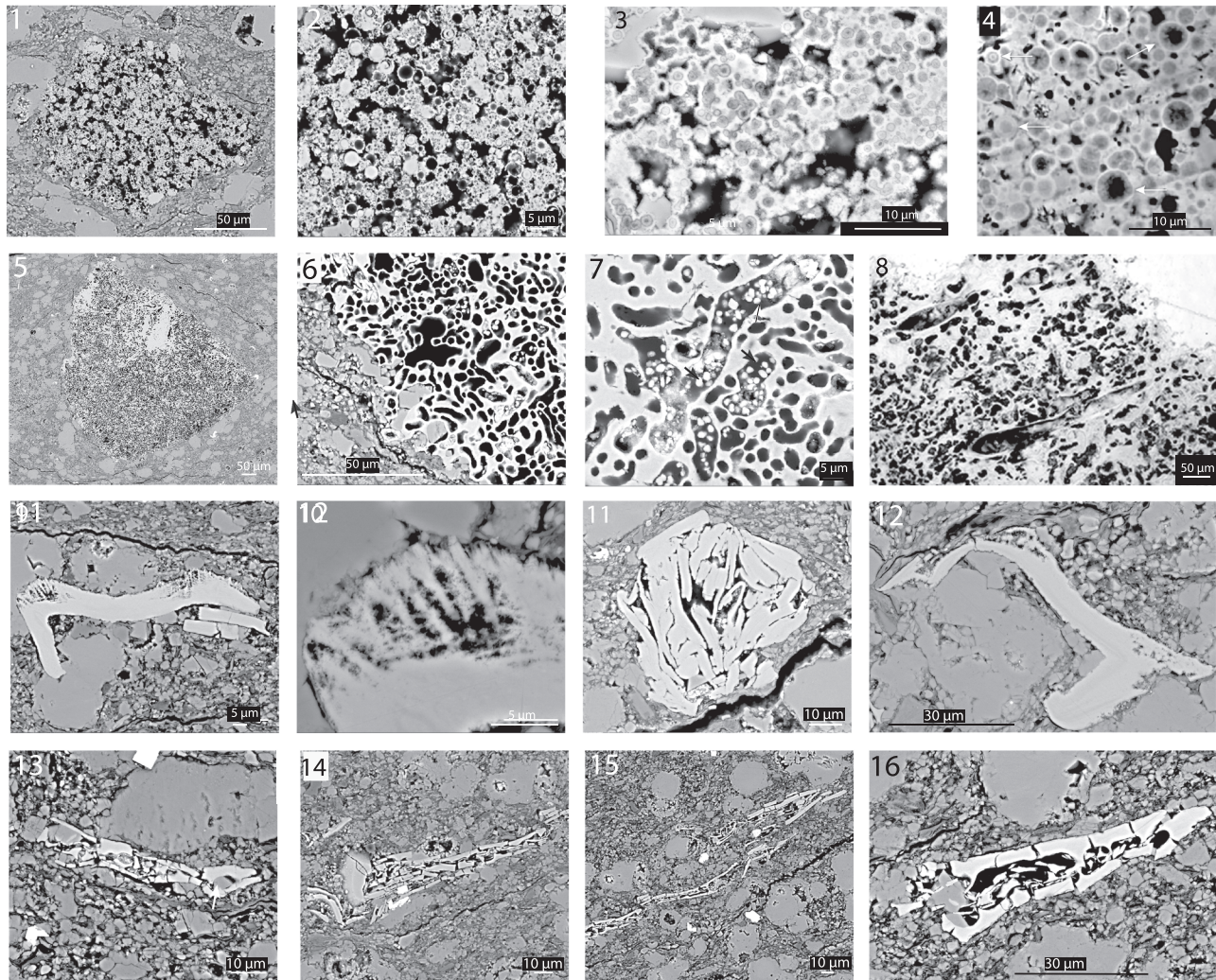
Figure 6. Backscattered electron (BSE) of apatite from the green marlstone including ancient and modern forms used for comparison. Pl. 1, 2, 3. Clusters of spherical fossil bacteria that resembles coprolites, Pl. 2 is close up of Pl. 1. Pl. 5–7. Piece of bone tunneled by cyanobacteria; Pl. 5. Whole object; Pl. 6, 7. Close up views of Pl. 5. Note apatite growing in pores in Pl. 7 (examples shown by arrow). Pl. 9–12. Layered and hooked specimens of possible marine arthropods. Pl. 13–16. Possible small fish fossils. Samples all in Core 40R-1, 32-34 cm. Pl. 1–7, 9–12. BSE images of thin sections. Pl. 4. Encrusted bacterial cells in hyaena coprolite from Pesquero et al. (2013, Figure 4C) (image available via a Creative Commons Attribution License, CC BY). Pl. 8. Brightfield reflected light image of section of an altered human bone tunneled by cyanobacteria from Hollund et al. (2018, Figure 6C) (image available via a Creative Commons Attribution License, CC BY). Scale bars on individual images.

A diverse array of microfossils composed of apatite are observed in thin section in the green marlstone between 616.58–616.56 mbsf: (1) 25- to 100-µm pellets consisting of micron-sized clusters of ellipsoidal to spherical forms, often showing concentric layers (Figure 6; Pl. 1–3; supporting information Figure S9; Pl. 1–4, 7–9); similar size and shaped objects often have round, ellipsoidal, and disk-shaped particles (supporting information Figure S9; Pl. 5, 10, 11, 13–16); (2) large (~600 µm) pieces of apatite with irregular, cylindrical pores often containing small apatite spheres (Figure 6; Pl. 5–7; supporting information Figure S9; Pl. 18–20); (3) arrangements of thin 1–5 (µm), elongated pieces of apatite in a skeletal-like structure (Figure 6; Pl. 13–16; supporting information Figure S10; Pl. 4, 6–8); and (4) more common 50 to 200 µm, elongate, often wispy blades or lenses of apatite with a subhorizontal orientation that are commonly fractured, hooked, and rarely coiled (Figure 6; Pl. 9–12; supporting information Figure S10; Pl. 1–3, 5, 9–30). Although the blades are largely recrystallized, their internal texture sometimes reveals discrete striations (200–800 nm in thickness) (Figure 6, Pl. 10; supporting information Figure S10; Pl. 22, 23). These objects are also rare in the lowermost transitional unit. The apatite blades appear to penetrate surrounding

sediment (supporting information Figure S10; Pl. 16, 17), indicating overgrowth or dissolution in the compacting sediment column, while carbonate grains continued to coalesce around them (Figure 6; Pl. 9).

3. Discussion

3.1. Origin of Micrite in the Transitional Unit and Green Marlstone

Samples in the upper part of the suevite contain very rare Ca-rich spherules and accretionary lapilli (Figure 1; Pl. 11) similar to those described in other K-Pg boundary sections (Yancey & Guillemette, 2008), areas of silicate melt and clay lenses that appear to be altered silicate impact melt (Figure 1; Pl. 10), and elliptical areas filled with mixed fine grained silicate and $CaCO_3$, likely carbonate ash-filled bubbles (Figure 1; Pl. 12; supporting information Figure S1; Pl. 11, 12; supporting information Figure S2; Pl. 7–12). The spherules and lapilli were part of the Chicxulub ejecta transported back to the crater by the tsunami. The highly angular shape and variable size of the majority of micrite in the transitional unit (Figure 1; Pl. 3–6) may be partially related to the lower energy of the seiche waves, but likely indicate a different origin.

Waters in the nascent Chicxulub crater would have been Ca-rich as a result of the interaction with the products of degassed target limestone and anhydrite; thus, it is possible that calcite could have precipitated directly from early crater waters. Calcite (and aragonite) precipitated from seawater in whitings or from fluids in hot springs shows regular prismatic or trigonal crystals (Jones, 2017; Thompson, 2000), very different from the irregular texture of micrite in the transitional unit. The transitional unit texture strongly resembles that of calcite derived by thermal decarbonation along fault zones (Collettini et al., 2013; Novellino et al., 2015) (Figure 7; Pl. 9 compare with Pl. 10) and experimentally (Hamann et al., 2018). Moreover, TEM images of a sample at 617.15 mbsf reveals regular ~100-nm-spaced lineations that resemble features in experimental decarbonation of Iceland spar (Rodriguez-Navarro et al., 2009) (Figure 7; Pl. 1–6 compare with Pl. 11, 12). These properties suggest that production of the angular micrite in the transitional unit involved decomposition of carbonate particles to CaO during shock devolatization followed by entrainment in the low-velocity ejecta at the final stages of excavation, rather than from the hot vapor-rich cloud. Models indicate solid particles will remain internal to the Chicxulub crater or be ejected just outside it in the final stages of crater excavation when ejection velocities are relatively slow (Kring, 2005). Externally ejected material would have been delivered to the peak ring site by resurge most likely via the breach in the crater rim to the northeast (Gulick et al., 2008). Subsequent carbonation or backreaction of CaO to $CaCO_3$ (Schulte et al., 2009) likely took place in the water column during suspension and settling; however, particles appear to have grown around grains such as apatite (Figure 6; Pl. 9, 13; supporting information Figure S10; Pl. 4, 5, 12), suggesting continued precipitation during early burial. The green marlstone also contains abundant micrite (supporting information Figure S11) along with clay and calcareous microfossils (Lowery et al., 2018). This micrite commonly shows a Moiré fringe in TEM (Figure 7; Pl. 7, 8) suggesting fine overlapping crystals. More diagnostically, the micrite strongly resembles micrite in the transitional unit showing low-order birefringence colors under cross-polarized light, likely as a result of the sheet-like nature of decarbonated calcite, and is distinct from micrite in the white limestone whose high-order birefringence colors resemble diagenetic calcite (supporting information Figure S11). This suggests that at least a fraction of the micrite in the green marlstone was also derived via backreaction in the water column, or possibly in the vapor plume (fine carbonate dust).

3.2. The Stratigraphic Significance of Charcoal Layers

The stratigraphic overlap of pyrite and charcoal and the preservation of wood structures (Figure 4; Pl. 1–8) suggest that the majority of pyrite replaced wood fragments transported into the crater from land or charcoalified during or after the impact process (Jones & Lim, 2000; Kruge et al., 1994), possibly through bacterial sulfate reduction. One hypothesized origin of charcoal is ignition of vegetation around the Gulf of Mexico by thermal radiation emitted by the impact plume or by wildfires ignited by ejecta heating the atmosphere (Gulick et al., 2019; Kruge et al., 1994; Melosh et al., 1990). The 10-cm-thick cross-bedded unit at the top of the suevite (Figure 2) was interpreted to be deposited by the reflected rim-wave tsunami, supported by the presence of soil-derived biomarker perylene in this otherwise marine sequence (Gulick et al., 2019). The position of the lower charcoal layers directly above this suggests that the charcoal and wood were also transported into the crater by the rim-wave tsunami and settled out more slowly than the sand fraction as energy declined (Gulick et al., 2019).
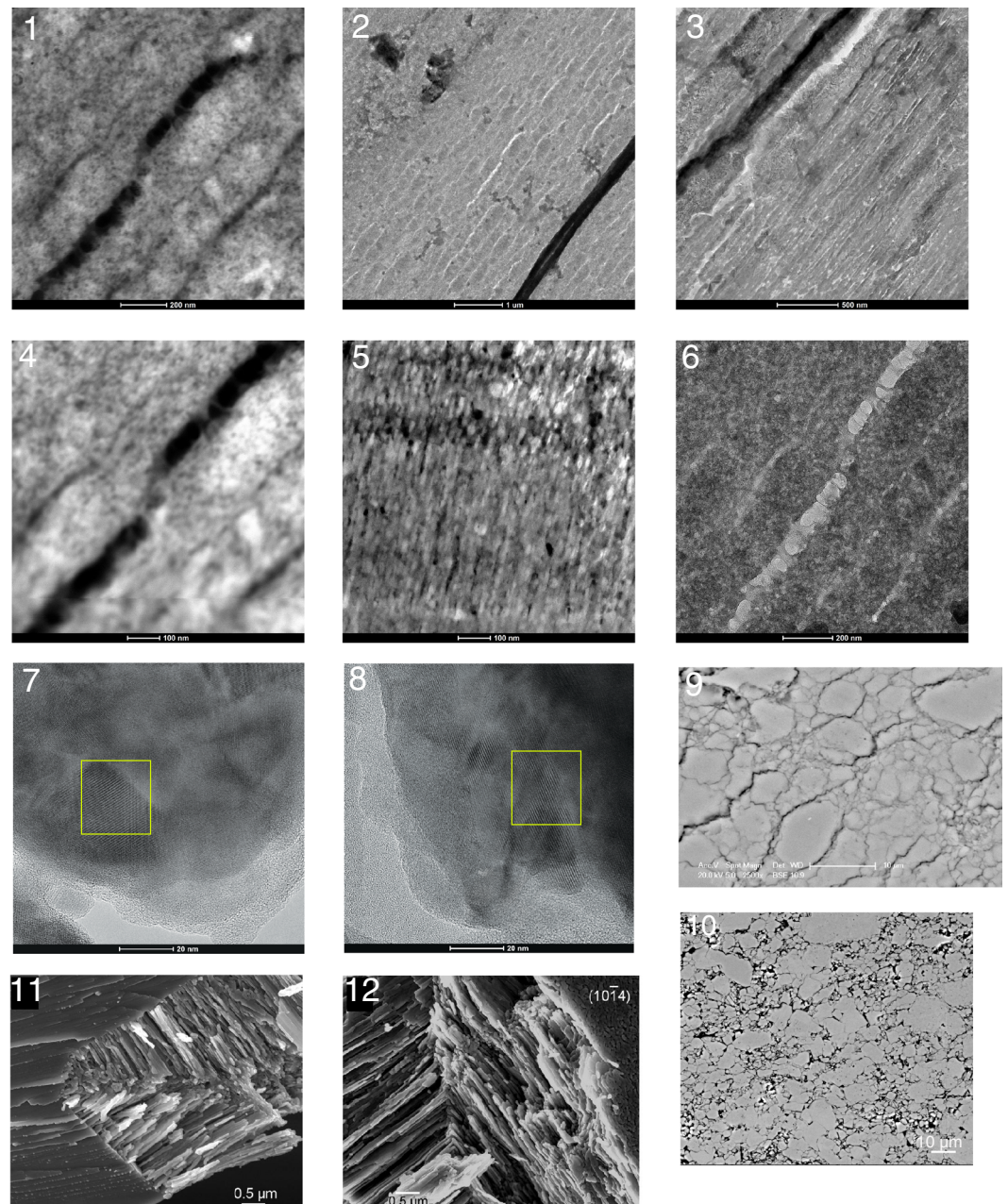
Figure 7. Transmission electron microscope (TEM) and secondary electron images showing ultrastructure of calcite in the transitional unit and comparison with calcite produced by thermal decarbonation; both classes of calcite shows planar features. Pl. 1–6 are of TEM micrographs of calcite in Sample 40R-1, 91 cm (617.13 mbsf). Pl. 7, 8 are of TEM micrographs of calcite in Sample 40R-1, 33 cm (616.57 mbsf) with Moiré fringe areas shown with insets. Pl. 9 is SEM of calcite in fault zone produced by thermal decarbonation (from C. Colletini, personal communication, January 3, 2019). Pl. 10 is backscattered electron (BSE) of 40R-1, 72–76 cm (616.94–616.98 mbsf). Scale bars in individual images. Pl. 11, 12 are SEMs of calcite produced by experimental thermal decarbonation from Rodriguez-Navarro et al. (2009). Images used with permission from the Mineralogical Society of America.

Pyritization can exaggerate the original charcoal abundance and create artificial bedforms, as in the case of the upper layers near the top of the green marlstone where the growth of large pyrite crystals outline what appears to be a ripple (Figure 3; Pl. 1, 2). In fact, finely dispersed pyrite is more or less evenly distributed along the layers. Although it is hard to rule out wood and charcoal derived from land, blades of pyrite (Figure 4; Pl. 1, 2; supporting information Figure S4; Pl. 5; supporting information Figure S5; Pl. 7–9) in

the thin uppermost (616.55 to 616.56 mbsf) layers (Figure 2) may be altered charcoal shards delivered by air-fall, a hypothesis proposed by Gulick et al. (2019) given that tsunami deposits would not be expected years after impact. This interpretation is supported by the overlap of the upper layers with the Ir anomaly which represents the atmospheric fallout of fine extraterrestrial material (Goderis et al., 2019), as does clay in the marlstone.

3.3. Duration of the Transitional Unit and Green Marlstone

Both chemical leaches show a significant decrease in micrite ^{87}Sr/^{86}Sr in the lower part of the transitional unit, with values significantly lower than the ^{87}Sr/^{86}Sr of contemporaneous global seawater at 66 Ma (MacLeod et al., 2001; Martin & Macdougall, 1991) (~0.707824–0.707832; Figure 5; supporting information Figure S6c). Hypotheses explaining the micrite ^{87}Sr/^{86}Sr values include vaporization of the impactor or target limestone (Belza et al., 2012). If micrite chemistry does indeed represent the local water column, as hypothesized above, then this suggests the impactor delivered enough Sr to the water column to alter its ^{87}Sr/^{86}Sr, though this is likely limited to the local basin (MacLeod et al., 2001). Assuming that (i) this shift was instantaneous, (ii) the impactor had an ^{87}Sr/^{86}Sr of ~0.703 (Dickin, 2018), and (iii) seawater Sr concentration is the same as modern (~90 μM), the impactor delivered ~6 · 10^5 mol of Sr to the local basin (this estimate would be higher if we accounted for active exchange with seawater and/or radiogenic hydrothermal inputs). If we assume an impactor volume of 525 km^3, and a density of 2 to 3 g/cm^3, appropriate for carbonaceous chondrite, we estimate an impactor mass of 1 to 1.6·10^{15} kg (Durand-Manterola & Cordero-Tercero, 2014). If the impactor had bulk Sr concentrations of ~5 to 15 ppm (Charlier et al., 2019; Faure & Powell, 1972; Wasserburg et al., 1969), then we would estimate that only a very small fraction (<0.001%) of the impactor would have had to solubilize. Alternatively, assuming ~200 to 600 ppm Sr in the target rocks (Schmitt et al., 2004; Tuchscherer, 2008), we estimate that >4·10^9 kg of solubilized rock could explain micrite ^{87}Sr/^{86}Sr; this estimate depends heavily on the assumption of the target rock ^{87}Sr/^{86}Sr, which could reasonably vary between ~0.70755 and 0.70765 (the latter of which is identical to the minimum micrite ^{87}Sr/^{86}Sr[65]). Regardless of source, ^{87}Sr/^{86}Sr of the transitional unit suggests an age close to that of the impact, consistent with ^{3}He isotope-based and biostratigraphic age controls (Lowery et al., 2018).

The ^{3}He technique assumes constant accumulation of cosmic-dust-derived ^{3}He in sediments and provides detailed interpretations of accumulation rate (Farley & Eltgroth, 2003). ^{3}He isotope data indicate extremely rapid deposition for the majority of the transitional unit (Lowery et al., 2018), and new measurements (supporting information) suggest a significant slowdown in rates in the uppermost few centimeters (Figure 2). Although the likely duration of the transitional unit is below the resolution for the technique, ^{3}He isotope data are consistent with the lower part of the transitional unit representing months, and the entire unit representing an interval no more than years, a duration that is consistent with the presence of the Ir anomaly beginning 2 cm from the top of the unit, indicating deposition within, at most, a few years. The slowdown in sedimentation rates continues in the green marlstone as the driver of deposition switched from waning impact energy and atmospheric fallout to hemipelagic sedimentation.

The age of the condensed green marlstone is more problematic as estimates derived from impact-derived materials are in apparent conflict with those from traditional biostratigraphy and ^{3}He isotope data. Impact-related materials include the peak of the Ir anomaly between 616.55 and 616.60 mbsf, the upper charcoal layers between 616.55 and 616.56 mbsf, very small (40–100 μm), altered, vesicular melt particles (supporting information Figure S2; Pl. 1–5), and, as discussed, possibly fine calcite dust, immediately below the upper charcoal layers (Gulick et al., 2019). The Ir anomaly generally signifies fallout within years of the impact (Artemieva & Morgan, 2009). These materials occur in a condensed 5 cm interval which contains the first occurrence, and high abundance, of *Parvularugoglobigerina eugubina* (whose appearance defines the boundary between Zones P0 and Pα) and other common incoming Paleocene planktic foraminifera. Estimates of the base of Pα range from ~30 kyr to as little as 3 kyr (Berggren et al., 1995) above the K-Pg boundary with considerable uncertainty (see Smit & Romein, 1985), a range that is consistent with ^{3}He isotope data.

The green marlstone is bioturbated (Lowery et al., 2018) and concentration of charcoal and wood in layers as well as the foraminiferal lags (Figure 3; Pl. 1) may be a result of minor winnowing, mixing materials from airfall, terrestrial, and pelagic sources. Ichnofacies indicates only a few cm of mixing at most

(Rodríguez-Tovar et al., 2020). Moreover, the apparent age dichotomy may be explained by upward remobilization of Ir and other platinum group elements in reducing pore waters (Colodner et al., 1992). However, the distribution of impact-related materials in the green marlstone, especially the lightest charcoal and woody material near the top, is also consistent with settling through the water column shortly after the impact. Particles in the green marlstone have a variety of sizes and would experience a range of settling rates (Maggi, 2013; Stokes, 1850). Finer material including clay (Lowery et al., 2018), abundant 1- to 2 μm-sized micrite (supporting information Figure S11; Pl. 4–6), and clay-sized pieces of charcoal and wood (Figure 4; Pl. 7, 8) would take several years to settle to the seafloor at 600-m water depth at 25°C and normal salinity. Large (>100 μm) pieces of charcoal and wood (e.g., supporting information Figure S3; Pl. 1) would take a few days to settle. Occurrence of larger charcoal particles near the top of the marlstone may have been a result of delivery to the seafloor via density currents following gradual settling of the underlying fines. Thus we conservatively interpret the marlstone to represent years to, at most, millennia. We therefore interpret the appearance of the earliest Paleocene planktic foraminifera in the crater in the immediate impact aftermath as part of a globally asynchronous recovery with ecological implications that are explored in a later section.

3.4. Evidence for Hydrothermal Circulation in the Early Crater

Heat and impact-induced rock fracturing and subsequent input of water at Chicxulub are thought to have generated a hydrothermal system, driven by the elevated temperatures of the melt sheet and uplifted lower crustal rocks in the crater center, that models suggest lasted for over 1.5–2.5 Myr (Abramov & Kring, 2007). Indeed, evidence for hydrothermal alteration is observed in granites and suevites at Site M0077 (Kring et al., 2020; Morgan & Gulick, 2018). Here we constrain the intensity of the hydrothermal system at the seafloor, and its impact on the crater environment, by determining temperatures and fluid chemistry during the deposition of the transitional unit and green marlstone using clumped, strontium and stable carbon and oxygen isotopes.

The isotopic composition of micrite would have been first imprinted at the time and site of carbonation, followed possibly by subsequent change during recrystallization to more stable forms in the sediment column. Traditional oxygen isotope temperatures measured on calcium carbonate ($\delta^{18}O_{CaCO3}$) are limited by uncertainty in the isotopic composition of the water in which precipitation took place. Assuming a seawater $\delta^{18}O$ value of −1.0‰, the traditional oxygen isotope thermometer indicates largely invariant temperatures of 41 ± 4°C (±values are 1 standard deviation of the pooled analyses) within the transitional unit, with higher temperatures in the underlying uppermost suevite (54 ± 2°C), and a return to normal ocean temperatures in the overlying pelagic limestone (22 ± 2°C) (Figure 5). The clumped isotope paleothermometer, however, is independent of assumptions about the isotopic composition of the water (Eiler, 2007; Ghosh et al., 2006) and thus is advantageous for determining the temperature of the early crater. Very rapid precipitation could result in metastable carbonates susceptible to recrystallization during early burial and, if so, the clumped isotope temperatures would reflect, at least in part, temperatures prevailing during recrystallization in the sediment column (Gabitov et al., 2012). Clumped isotope-based temperatures are 73 ± 13°C (1σ) with no clear trends for most of the transitional unit (Figure 5) and decrease within the green marlstone to 27 ± 7°C in the overlying Danian foraminiferal limestone.

Together with $\delta^{18}O_{CaCO3}$ values, the clumped isotope temperatures permit calculation of the apparent isotopic composition of water ($\delta^{18}O_w$) in which carbonates formed. For the transitional unit, this approach yields a mean $\delta^{18}O_w$ value of +4.3 ± 1.9‰ (Figure 8). This value is ~3 ‰ higher than any plausible open-ocean surface $\delta^{18}O$ value for the latest Cretaceous. We offer two end-member scenarios that could result in such high apparent $\delta^{18}O_w$ values. In the first scenario (Figure 8a), the high values represent actual water isotopic compositions, with the water being enriched in ^{18}O due to extensive evaporation of seawater from heat generated by the impact event, or via high-temperature exchange with rock-derived O (which is enriched in ^{18}O relative to seawater) from the water circulating through the impact melt rocks and suevite (or a combination of both). In this scenario, the ~70°C clumped isotope temperatures of the transitional unit reflect actual water temperatures during initial carbonate mineralization in the water column or during early burial. This scenario is possibly supported by the occurrence of evaporite minerals in the upper and lower transitions (Figure 9; Pl. 1–6, 8, 9; supporting information Figure S12; Pl. 1–3; see supporting information). These minerals could be precipitates from local evaporation of seawater at the time of impact or trace residual of the target rocks.
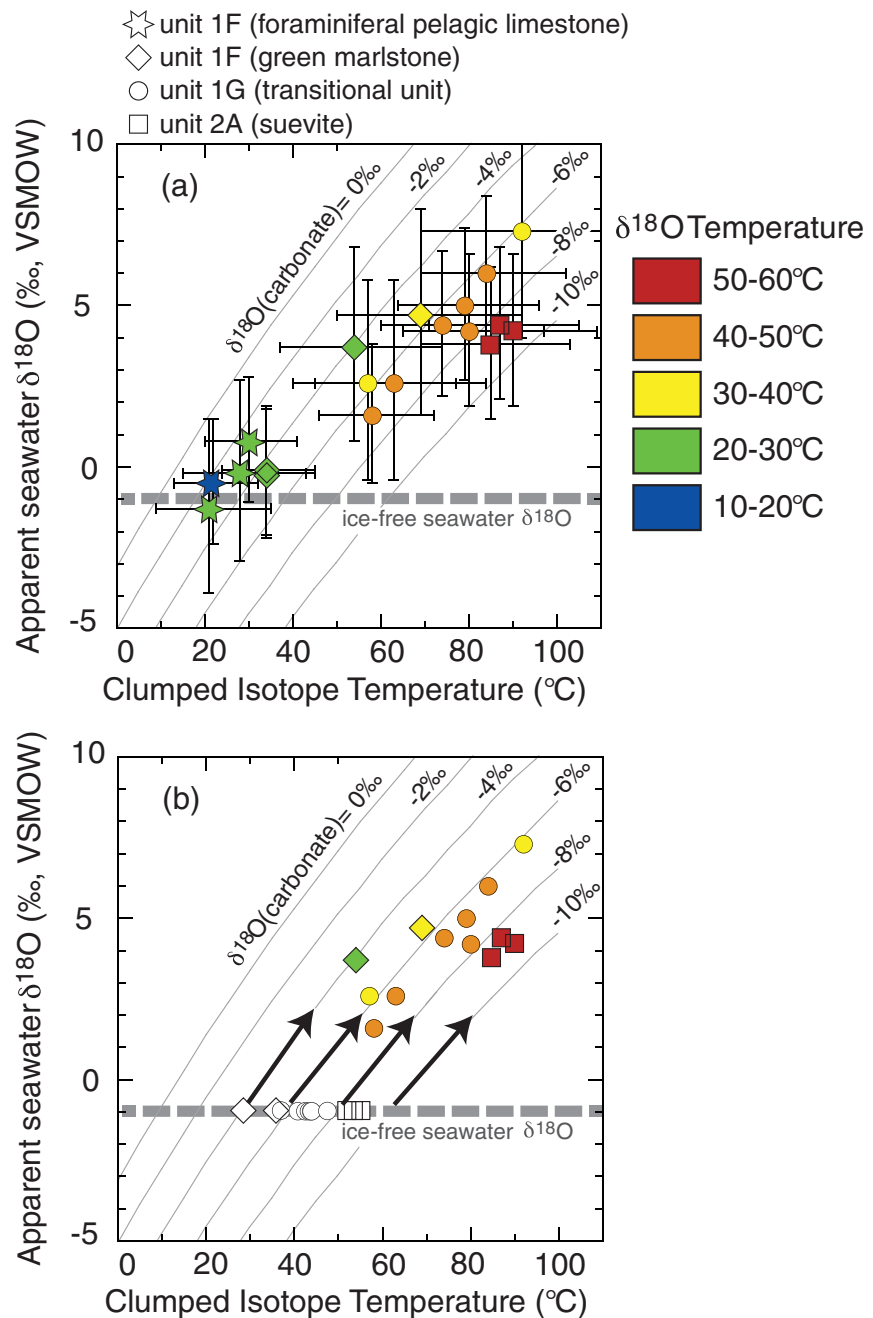
Figure 8. (a) Apparent seawater δ^{18}O versus clumped isotope temperature, contoured for constant $\delta18$Occ (thin gray lines). The apparent seawater δ^{18}O values are calculated using the oxygen isotope thermometer of Kim and O'Neil (1997), with temperatures based on clumped isotopes. The color scale indicates the traditional oxygen isotope-based temperatures under the assumption that δ^{18}Ow = −1‰. (b) Illustration of the scenario where the initial carbonate forms in cooler (but still extremely warm) seawater with δ^{18}O = −1‰ (white symbols), and subsequently recrystallizes on the higher-temperature seafloor under rock-buffered (δ^{18}O-preserving) conditions (black arrows). Such recrystallization results in increased clumped isotope temperatures but little or no change in δ^{18}Occ, which results in apparent seawater δ^{18}O values that are erroneously high.

In a second scenario (Figure 8b), the carbonates initially formed in seawater of "normal" δ^{18}O (~−1‰) at temperatures indicated by the oxygen isotope thermometry (generally in excess of 30°C but cooler than 60°C). During early burial on the warmer seafloor, the carbonates recrystallized under rock-buffered conditions (low water/rock ratio with respect to oxygen atoms) such that the clumped isotope temperatures
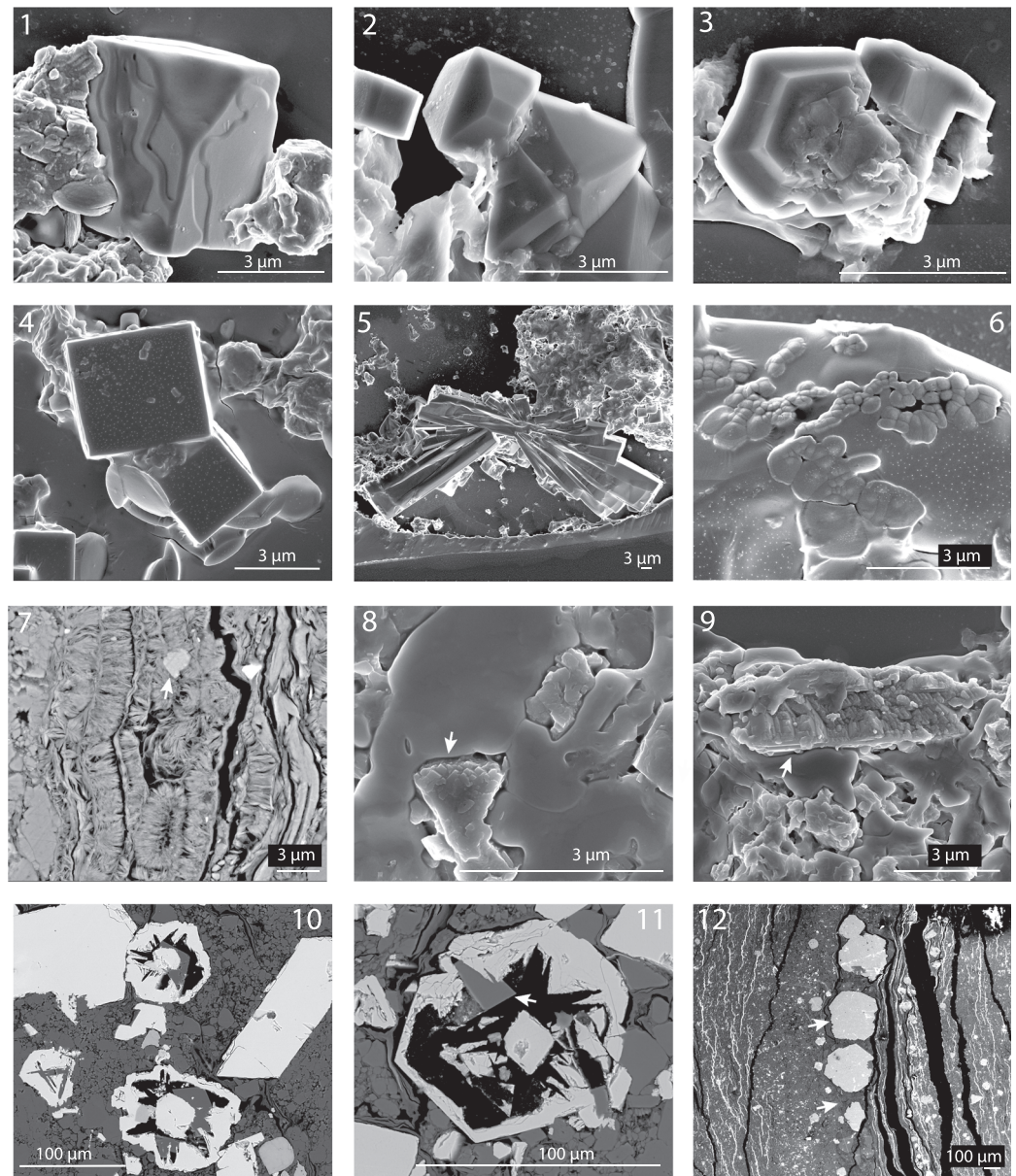
Figure 9. Backscattered electron (BSE) and secondary electron images of anydrite, halite, apatite, ZnS, and pyrite from the transitional unit and green marlstone. Pl. 1, 4, 6. Halite. Pl. 2, 3, 5. Anhydrite. Pl. 7. Apatite (arrow) in chlorite vein. Pl. 8, 9. Apatite (arrows) surrounded by halite. Pl. 10–11. ZnS (light gray) with calcite (dark gray shown by arrow) crystals inside. Pl. 12. Pyrite crystals (upper arrow) in chlorite (lower arrow) vein. Samples all in Core 40R-1: Pl. 1, 4, 6. 31 cm (616.55 mbsf); Pl. 2, 3, 5. 108 cm (617.32 mbsf); Pl. 7, 12. 106–108 cm (617.30–617.32 mbsf). Pl. 8, 9. 110 cm (617.34 mbsf); Pl. 10, 11. 67-72 cm (616.91–616.96 mbsf); Pl. 7, 10–12. BSE images of thin sections; Pl. 1–6, 8, 9. Secondary electron images of strewn slides. Scale bars on individual images.

recorded by carbonates increased, but the $\delta^{18}O_{CaCO3}$ value remained largely the same. This pattern is commonly seen in clumped isotope studies of diagenetically altered carbonate sediments (Ferry et al., 2011; Henkes et al., 2014; Shenton et al., 2015) and results in fictive $\delta^{18}O_w$ values that are higher than plausible seawater values. Under this scenario, the actual seafloor temperatures were at least as high as the temperatures recorded by clumped isotopes (73 ± 13°C); if the carbonates were not completely recrystallized at this time (i.e., if they retained some of the isotopic signature attained prior to burial), then seafloor temperatures must have been even higher. We disfavor this in situ high-temperature alteration scenario for three reasons. First, as discussed in more detail below, heat flow models suggest

that the >130-m-thick mantle of tsunami and suevite deposits overlying the impact melt rock on top of the peak ring and even thicker deposits overlying the impact melt sheet in the central basin would have functioned as a highly effective thermal insulator, resulting in temperatures similar to overlying seawater temperatures. Seawater temperatures, in turn, would largely reflect "normal" Gulf water temperatures because the volume of distal Gulf water rushing back to the impact site following the impact event would have been vastly larger than the volume of (initially very hot) water in the immediate vicinity of the impact. Additionally, the presence of clear indicators of pelagic and benthic life in the upper part of the transitional unit suggests that water temperatures at the time these sediments were deposited were not too extreme for life. Finally, and critically, the clear decrease in C-isotope values in the interval of soft sediment deformation demonstrates that C-isotope values were acquired prior to burial, that is, represent water column values (Figure 5) and this interpretation is supported by the lack of textural difference in micrite in this interval (supporting information Figure S1; Pl. 3).

We also disfavor interpretations invoking kinetic fractionation as the primary explanation of the stable isotope data. The clumped isotope data do not record the extremely high-temperature processes within the initial vapor plume that would have prevailed during decarbonation and possibly during recarbonation in the plume. Mass independent triple oxygen isotope fractionation ($^{17}O/^{16}O$ relative to $^{18}O/^{16}O$) during decarbonation has been shown experimentally (Miller et al., 2002), with CO_2 anomalously enriched in ^{17}O and CaO anomalously depleted, with differences in $\Delta^{17}O$ of ~400 per meg between the two phases. High-precision triple oxygen isotope measurements of a sample from the transitional unit and a sample from the overlying Danian foraminiferal limestone show no significant deviation from compositions expected for equilibrium with seawater (supporting information Figure S12 and Supporting Information S1), indicating that the carbonates do not contain O inherited from the precursor CaO or CO_2 generated in the impact plume, unless the recombination was fortuitously stoichiometric, such that the negative and positive $\Delta^{17}O$ anomalies precisely canceled. Carbon isotope compositions show no evidence of kinetic fractionation and are within the range expected for latest Maastrichtian and earliest Danian carbonates. Finally, timescales for oxygen exchange between DIC and water are extremely rapid at elevated temperatures; for example, at 50°C, $t_{1/2}$ = 420 s for HCO_3^--dominated solutions, and $t_{1/2}$ = 11.5 h for CO_3^{2-}-dominated solutions, based on kinetic data from Beck et al. (2005). Therefore, carbonate formation would need to be extremely rapid in order to incorporate DIC in isotopic disequilibrium with seawater. If the carbonate growth were this rapid, the resulting carbonates would likely be metastable (poorly ordered, high surface area) and hence susceptible to isotope exchange during recrystallization. Collectively, these lines of evidence argue against a strong kinetic fractionation signal preserved in isotopic compositions of the transitional unit carbonates.

The initial resurge flooded the >1-km-deep impact basin, covering the peak ring with ~600 m of relatively cool Gulf of Mexico waters (Lowery et al., 2018). The 130-m-thick suevite section at Site M0077 would have thermally isolated the deep waters from the underlying granitoid rocks and impact melt during the deposition of the transitional unit as conduction would have been too slow to warm even the bottom of the ocean. The central melt sheet, which is over 10 km from the peak-ring site and covered by several hundred meters of suevite (Abramov & Kring, 2007), also cannot have maintained warmer water temperatures within the entire impact basin during the formation of the transitional unit. Thus, we postulate that the carbonation took place nearer to the central melt sheet where deep waters would have been heated by interactions with melt as well as via ejection of hot fluids at hydrothermal vents. Precipitation of carbonate in such an environment would have been promoted not only by the returning CaO flux but also by the decreased solubility of carbonate in the high-temperature waters (He & Morse, 1993; Mucci, 1983; Plummer & Busenberg, 1982) and by increased rates of backreaction in such waters (Agrinier et al., 2001). Thus, regardless of origin, seawater in proximity of the central melt sheet may have precipitated voluminous micrite, a literal carbonate "factory" (Figure 10a). Yet CaO ejecta and subsequent backreaction would have been crater-wide and likely greater, as resurge and later seiches transported these ejecta back into the crater. Thus, it is likely that transitional unit micrite was derived from a wide region but with a larger proportion from waters near the central melt sheet. We thus view the clumped isotope values in the transitional unit as representing some of the warmest, but possibly not the highest temperatures in the nascent crater.
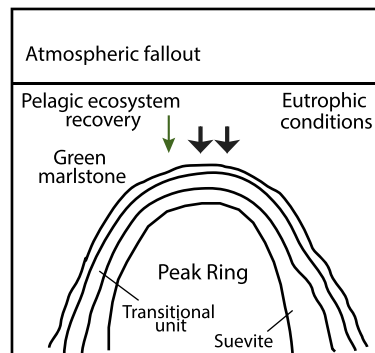
Hydrothermal venting near the central melt sheet would have been widespread and intensive (Abramov & Kring, 2007). Such venting would leave an imprint on the trace element chemistry of the waters in which the transitional unit micrite formed. The abrupt increase in $^{87}Sr/^{86}Sr$ above 616.65 mbsf (Figure 5)
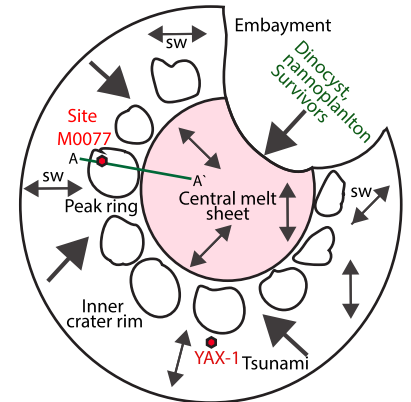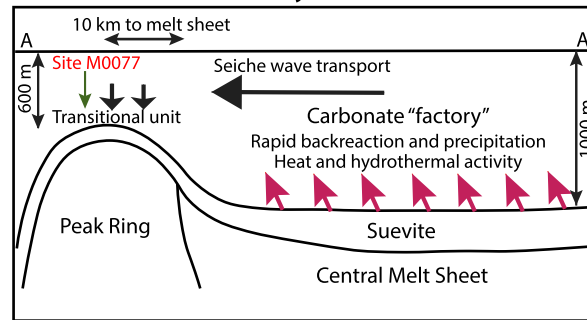
Figure 10. Cartoon showing proposed origin of the transitional unit and green marlstone. (a) Upper row—deposition of transitional unit showing cross section (left) and birds-eye view (right). Red arrows in section indicate convection from central melt sheet; thick black arrows show direction of seiche wave transport and deposition of $CaCO_3$ in transitional unit at Site M0077; location of Site M0077 indicated by green arrow. Birds-eye view shows whole crater with opening to the Gulf of Mexico to the northeast and morphological features including the peak ring; seiche waves indicated by double ended arrows; tsunami waves by single arrows. Location of M0077 and YAX-1 indicated by red symbols; green line indicates section in Panel A. Site water depth after Lowery et al. (2018). (b) Lower row—deposition of green marlstone at Site M0077 showing atmospheric fallout combined with eutrophic conditions.

occurred over intervals of years to, at most, millennia, as argued above. This is more rapid than rates of evolution of seawater $^{87}Sr/^{86}Sr$ which are much slower as reflected by the residence time (5 million years) and cannot be a consequence of mass delivered by the impactor. Assuming an estimated mass of water of ~$1.6 \cdot 10^{11}$ kg (180 km diameter, 1 km average depth) in the local basin, an ~100-year time frame and a moderate amount of exchange with seawater (i.e., the water residence time in the crater is ~0.05 to 1 year) suggests a Sr mass flux of ~10^6 to $2 \cdot 10^7$ mol Sr/year and a crater water column Sr concentration that increases by 7%. The rate of change at Site M0077 must therefore reflect local input of radiogenic Sr, possibly from hydrothermal alteration of underlying crust, consistent with clumped isotope temperatures. The impact melt sheet is thought to have an average (granitic) crustal composition (Kring, 1995), suggesting that the micrite $^{87}Sr/^{86}Sr$ reflects a water column that is influenced by the hydrothermal alteration of granitic composition rocks near the central melt sheet. Significantly from a stratigraphic viewpoint, the ordered progression of Sr isotope ratios indicates a gradually evolving crater chemical system as well as a batch-like supply of micrite to the peak ring site.

The acetic-soluble $^{87}Sr/^{86}Sr$ trend is broadly comparable to those of Fe/Ca and Mn/Ca (supporting information Figure S6b), and both trace elements are enriched throughout most of the transitional unit, consistent perhaps with higher temperatures. In addition, Mg/Ca values are ~11 to 14 mmol/mol in the transitional unit (and only ~20 mmol/mol in the HCl-soluble fraction), which are considerably higher than biogenic

carbonates. Assuming recent constraints on the equilibrium partitioning behavior of Mg into calcite (Lammers & Mitnick, 2019) are appropriate, and that the measured Mg/Ca reflects inorganic $CaCO_3$ precipitation, pore fluid Mg/Ca would have to be extremely low (<0.1) to explain these values. Such a low value is consistent with hydrothermal input that is Mg-poor, such as might be expected in a granite-hosted system.

The transitional unit also contains the following mineralogical evidence of in situ hydrothermal alteration: (1) Isolated grains of ZnS are observed in the upper pyrite layers at the base of the green marlstone (616.56 to 616.55 mbsf) and in a thin chlorite vein in the transitional unit at 616.96 to 616.91 mbsf (Figure 9; Pl. 10, 11; supporting information Figure S5; Pl. 11, 12; supporting information Figure S12; Pl. 4–6), at 617.28 to 617.26 mbsf, at 617.34 to 617.32 mbsf, and at 617.54 to 617.49 mbsf. (2) At the basal contact of the transitional unit (617.33 to 617.3 mbsf), pyrite appears to occur in veins filled with chlorite and minor calcite that resemble fluid escape structures (Morgan & Gulick, 2018) (Figure 3; Pl. 7; Figure 9; Pl. 12; supporting information Figure S12; Pl. 7–11). The occurrence of these sulfides in veins suggests that they precipitated directly from hydrothermal fluids, clearly a distinct origin from the subhorizontal charcoal-derived pyrite layers. This is consistent with sulfur isotope data, which suggests high and low temperature generation of pyrite (Goderis et al., 2019). The occurrence of chlorite suggests pore water temperatures in excess of 300°C, which is consistent with independent temperature estimates (Kring et al., 2020). (3) Wood petrified by phosphatization and silification (Figure 4; Pl. 10–12) also indicates alteration by fluids, although this process can occur at low temperature (Akahane et al., 2004). (4) Small grains of apatite are also observed within chlorite veins (Figure 9; Pl. 7). Apatite is a common phase in pegmatites as P and Ca are concentrated in late-stage magmatic fluids. Thus, we suggest that these apatite grains also precipitated from hydrothermal fluids.

The occurrence of pyrite in chlorite veins and ZnS within the transitional unit and at the base of the overlying green marlstone indicate thin fingers of higher temperature fluids penetrated the buried sediment column and that local hydrothermal activity persisted possibly a for long time after normal hemipelagic deposition resumed consistent with models showing a long-lived hydrothermal system at Chicxulub (Abramov & Kring, 2007). Clumped isotopes place constraints on the integrated temporal duration of this hydrothermal fluid flow, because internal clumping in carbonate minerals is susceptible to resetting via solid-state diffusion at elevated temperatures. For sustained heating at 300°C, kinetic models predict that clumped isotopes will inherit the 300°C signature in 10^1 to 10^7 years (Brenner et al. (2018), Table 5). At 275°C, approximately 10^2 to 10^8 years would be required for inheritance of the 300°C signature. The fact that clumped isotopes record far cooler temperatures (88 ± 11°C and lower) indicates that the duration of transitional unit hydrothermal activity was brief, a few years or less, or that fluid temperatures were cooler than suggested by the presence of chlorite, or both.

Clumped isotope temperatures abruptly decline near the top of the transitional unit between 616.635 and 616.605 mbsf to assumed sea surface temperatures of 27 ± 7°C within the green marlstone (Figure 5). This change is coincident with the switch from material transported from warmer regions of the crater to hemipelagic deposition (Figure 10b) yielding temperatures that can be interpreted as in situ surface water values from plankton and backreacted calcite. In fact, we postulate that surface temperatures at the peak ring site remained within a few degrees of this level during the deposition of the transitional unit and that this location was representative of surface water conditions for much of the crater given its limited size. In the following we explore how the unique crater environment, involving hydrothermal activity, allowed life to recover and flourish in the immediate postimpact environment.

3.5. New Evidence for Life in the Nascent Crater

Globally, data and models suggest that the first decades after the impact were characterized by low light and impact winter (Artemieva & Morgan, 2017; Brugger et al., 2017; Kaiho et al., 2016; Lyons et al., 2020; Tabor et al., 2020; Vellekoop et al., 2014). However, our results indicate that waters in the crater remained warm in the immediate postimpact interval, possibly as a result of hydrothermal activity, even with the possibility of low light levels as suggested by evidence for atmospheric fallout. Here we compare this environmental record with evidence for return of life to the crater (Lowery et al., 2018).

Site M0077 contains a remarkable fossil record that illustrates rapid colonization of the newly formed crater by organisms representing a range of trophic levels (Figure 11). Survivor species of nannofossils and planktic foraminifera are generally rare throughout the transitional unit (as might be expected with such
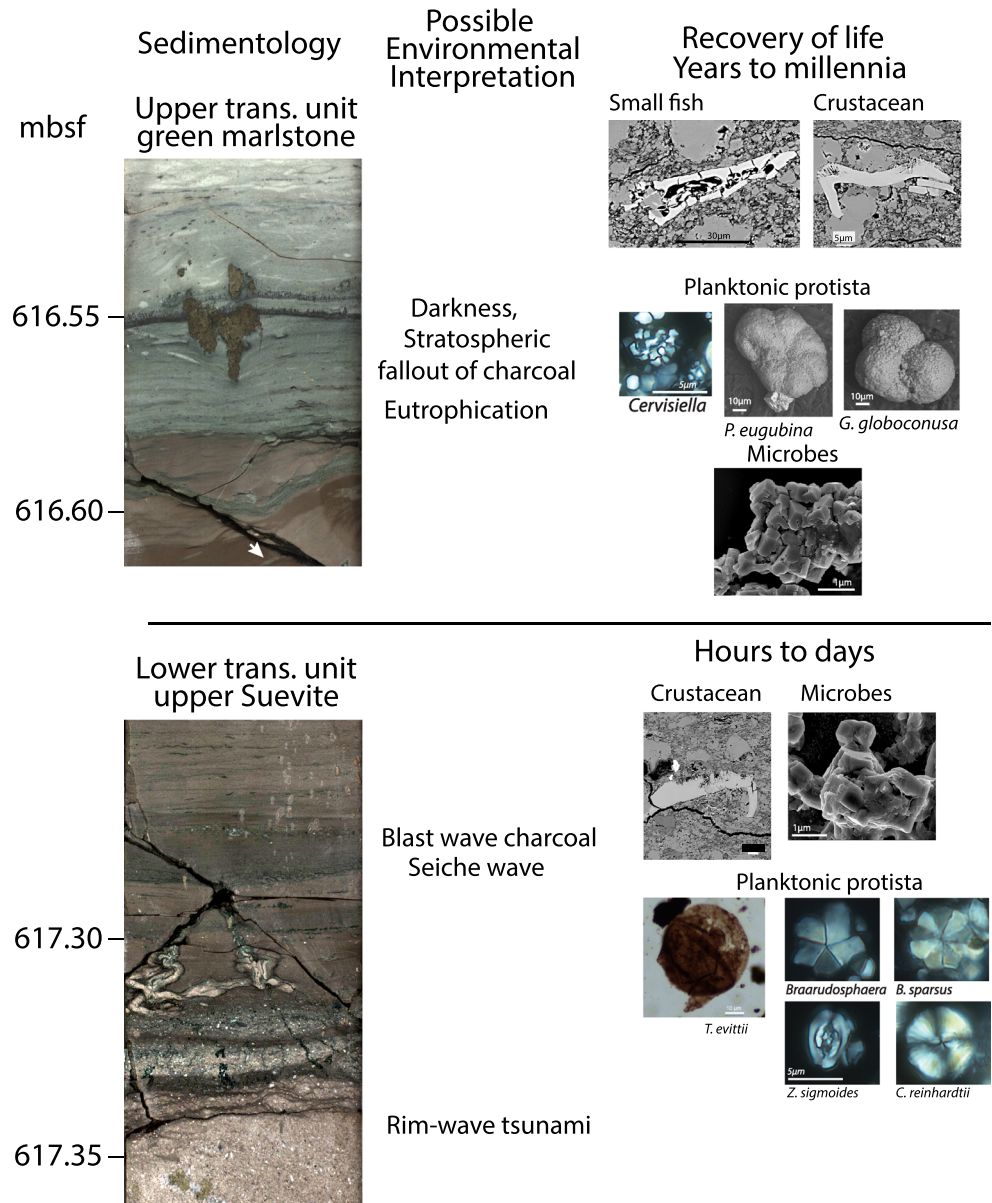
Figure 11. Recovery of life and its relationship with environment in the nascent crater. At left is sediment core showing lowermost and uppermost transitional unit and green marlstone and its environmental interpretation. At right are fossil occurrences at various trophic levels and timing of the recovery. Higher orders include apatite remains of small fish and pelagic crustaceans. Planktonic protistans are represented by planktic foraminifera, calcareous nannoplankton, and dinoflagellates. Microcystals that appear to be made by cyanobacteria (Bralower et al., 2020). Scale bars by individual images (bars by *Z. sigmoides* pertains to four nannofossil images).

rapid depositional rates), although they increase in relative abundance upsection (Lowery et al., 2018). Planktic foraminifera and nannofossil assemblages include significantly older (late Campanian-early Maastrichtian) species, particularly near the base of the transitional unit, indicating that at least part of the assemblage is reworked from older beds. Lowery et al. (2018) interpreted the gradual increase in the abundance of planktic foraminiferal and calcareous nannoplankton survivors at the top of the transitional unit as evidence for the return of life to crater surface waters, and the presence of burrowing organisms as an indication of a habitable sea bed. Here we focus on samples from the lowermost transitional unit (617.24 to 617.3 mbsf) and the uppermost transitional unit and the green marlstone (616.6 to 616.545 mbsf). These intervals represent lower-energy conditions as tsunami and seiches waned (lowermost

transitional unit) and suspended material settled out and potentially less redeposition combined with a larger in situ component (uppermost transitional unit and green marlstone). Both intervals might contain minor hiatuses, but there is no evidence for a significant gap in deposition.

The lowermost transitional unit contains survivor nannoplankton *Braarudosphaera* spp., *Cyclagelosphaera reinhardtii*, and *Zeugrhabdotus sigmoides* (Figure 11; supporting information Figure S7), taxa that are generally rare in uppermost Maastrichtian samples but become common to abundant immediately above the boundary. Specimens are rare but far exceed typical Late Cretaceous sample abundance; thus, their occurrence is interpreted as significant. The occurrence of *Biantholithus sparsus* is surprising and also significant. This species which is commonly used as a marker for the K-Pg boundary has been observed below the boundary only at one site likely as a result of bioturbation (Pospichal & Wise, 1990). The dinoflagellate cyst *Trithyrodinium evittii* also originates and is very rare in the latest Maastrichtian (Pospichal & Wise, 1990; Vellekoop et al., 2018) but becomes a disaster taxon in the earliest Danian where it is highly abundant (Vellekoop et al., 2018). Nannoplankton assemblages in the green marlstone are very different, dominated by a primitive form of *Cervisiella* spp. (commonly known as *Thoracosphaera;* supporting information Figure S7; Pl. 7, 8), which is a cyst of a calcareous dinoflagellate (Brinkhuis & Zachariasse, 1988) and this taxon continues to dominate samples in the overlying white limestone (Jones et al., 2019). There are no organic-walled dinoflagellates in the green marlstone but calcite and apatite interpreted as fossils of cyanobacteria are common (supporting information Figure S8; Pl. 1–8), an interpretation supported by organic biomarkers (Schaefer et al., 2020).

Nannoplankton and palynomorphs are highly susceptible to reworking, especially by high-energy transport processes such as tsunami and seiches. Although the lowermost transitional unit contains common reworked Cretaceous species, the abundance of typical early Danian taxa including the survivors *Biantholithus sparsus* and the dinoflagellate *T. evittii* suggests that at least part of the assemblage represents early recovery either in waters outside the crater and subsequently transported in by tsunami or possibly within the crater as tsunami energy subsided (Figure 11). Species in this interval are dominated by haptophytes that grew in the photic zone, indicating sunlit surface oceans, and the dinocyst *T. evittii* is considered to be heterotrophic (Brinkhuis et al., 1998), which indicates food supply from primary producers, possibly nannoplankton or cyanobacteria. The primary nannoplankton and dinoflagellate species in the lowermost transitional unit are an unexpected discovery: direct survivors that thrived in or around the nascent crater even as tsunami energy waned.

By contrast, the abundance and unusual form of *Cervisiella* in the green marlstone, coinciding with the lowest occurrence of a number of incoming planktic foraminifera, including *P. eugubina* (Lowery et al., 2018), is accompanied by near absence of Cretaceous taxa, suggesting that nannofossils represent an in situ true recovery biota (Figure 11). Moreover, the distinct nature of nannofossil assemblages from the lower and upper transitions suggests a primary environmental change between these stages of the crater recovery. *Cervisiella* spp. is a dinoflagellate cyst, one of the "disaster" taxa that was adapted to harsh environments and formed oceanwide blooms in the extinction aftermath (Jones et al., 2019). The assemblage from the lowermost transitional unit disappeared, suggesting that conditions had likely deteriorated to the point where surface oceans were uninhabitable for almost all haptophyte nannoplankton and other dinoflagellates. The green marlstone assemblage is unique; the lowermost samples at other proximal sites with expanded records contain a mixture of *Cervisiella* spp. and other survivors (Jiang et al., 2010), likely because they derive from a higher stratigraphic level or are mixed by bioturbation or winnowing.

The environmental significance of flora and fauna in the green marlstone depends on the interpretation of impact-derived materials. At face value, the co-occurrence of the Ir anomaly, charcoal, and impact spherules supports the conclusion that these impact derived materials and microfossils are in situ. In this case, we speculate that the nearly monogeneric *Cervisiella* assemblages were a response to low light levels from dust and soot, a finding that would represent a compelling link between one of the "kill mechanisms" and the plankton record. If the planktic foraminifera in the green marlstone are also in situ, and not mixed relative to the impact-derived materials, then it is possible that survivors and a dozen new taxa originated within years of the impact which is unlikely, but not impossible. Even a few thousand year-long recovery, the maximum likely age for the green marlstone as discussed earlier, is far more rapid than has been observed at other continental margin and open marine sites (Birch et al., 2012; Coxall et al., 2006). Either age interpretation would

imply that conditions in crater waters were suitable for recovery enabling a suite of planktic foraminiferal species to thrive before they were able to elsewhere. How can this rapid recovery be explained?

The fossil record of the green marlstone, regardless of age interpretation, illustrates that as calcareous phytoplankton were experiencing harsh surface ocean conditions in the nascent crater, coexisting planktic foraminifera were recovering, even thriving (Lowery et al., 2018). Planktic foraminifera would have required an alternative food source given the decimation of the calcareous nannoplankton, their primary source in the Cretaceous. Possibilities include diatoms and dinoflagellates which suffered lower extinction rates (Hull et al., 2011), although neither group is found in the green marlstone. The occurrence of calcite and apatite microcrystals in the green marlstone are interpreted as precipitates induced or influenced by cyanobacteria (Bralower et al., 2020; Schaefer et al., 2020), and thus a burgeoning microbial community may also have served as food for the recovering planktic foraminiferal community and other zooplankton in the crater (Bralower et al., 2020).

Perhaps the most remarkable aspect of the crater fossil record is the discovery of a diverse assemblage composed of apatite, predominantly at the base of the green marlstone but with a few specimens at the base of the transitional unit (Figure 6; supporting information Figures S9 and S10). Identification of the small fragments of fossil apatite is difficult, especially since specimens appear to have been heavily overgrown, but resemblance with modern and other fossil materials provides some clues. (1) The clusters of ellipsoidal and spherical forms strongly resemble fossil bacteria in coprolites in size and form (Figure 6; Pl. 1–3 compare with Pl. 4) and the pellet structures (supporting information Figure S9; Pl. 5, 10, 11, 13–16) resemble more modern fecal pellets from a terrestrial site (supporting information Figure S9; Pl. 6, 12) (Al-Bassam & Halodová, 2018; Cosmidis, Benzerara, Gheerbrant, et al., 2013; Cosmidis, Benzerara, Menguy, et al., 2013; Pesquero et al., 2013; Pineda et al., 2017; Zatoń et al., 2015). (2) The large pieces of apatite are more difficult to assign because they are heavily altered. The random shape and orientation of cavities differ from known biogenic materials such as bone or dentin. Their size and the occurrence of small apatite spheres resemble highly altered bone fragments that have been tunneled by cyanobacteria (Ramírez-Reinat & Garcia-Pichel, 2012) (Figure 6; Pl. 5–7 compare with Pl. 8; see also supporting information Figure S9; Pl. 18–20) (Atkins et al., 2014; Cohen et al., 2012; Emslie et al., 2015; Seidel et al., 2016). (3) The apatite blades are also heavily overgrown and most of their original structure has been erased. However, obvious striations in some of these blades do appear to be primary structures (Figure 6; Pl. 9, 10; supporting information Figure S10; Pl. 9, 10, 14, 15), and blades are often clustered (Figure 6; Pl. 11; supporting information Figure S10; Pl. 1, 2). The blades, including those in clusters, are generally hooked, with claw-like protrusions on the ends, and resemble crustacean (e.g., copepod) appendages in size, segmentation, and shape. Burial may have compressed the blades into the layered clusters. Crustacean appendages are originally chitinous and have the potential to become phosphatized (Xiao & Schiffbauer, 2009) and the underlying chitin structure can appear striated (Astrop et al., 2015), although commonly occurring in spindles (Chandran et al., 2016). (4) The delicate layered structures (Figure 6; Pl. 13–16; supporting information Figure S10; Pl. 4, 6–8) also resemble fossil bone, which may have come from small fish living in the crater. Fossilized bone is often recognized by preservation of osteocyte lacunae, although numerous fish lineages bone can also be acellular (Horton & Summers, 2009). As these structures are only 10–100 μm in size, they may represent juvenile or small adult mesopelagic fish, rather than large predatory individuals. Selective survival and rapid radiation of pelagic fishes, particularly small mesopelagic taxa is known to have occurred following the K-Pg (Alfaro et al., 2018; Friedman, 2009; Sibert & Norris, 2015), so early recolonization by these taxa is quite possible. Fish only experienced moderate levels of extinction at the K-Pg event, and fish debris, including teeth (Sibert et al., 2014), are common in both marine and continental K-Pg boundary clays, including the classic Stevns Klint Fish Clay K-Pg outcrop in Denmark (Forchhammer, 1825) and the recently described Hell Creek section in North Dakota (DePalma et al., 2019). We speculate that the coprolites, blades and the piece of bone recovered from the sediments within the Chicxulub crater represent the remains of pelagic metazoans, perhaps crustacean zooplankton (e.g., copepods) and possibly fish that survived the extinction and were able to capitalize on the earliest Danian phytoplankton food webs. The green marlstone may represent a unique preservational environment where the combination of pore water euxinia and limited burrowing activity enabled the phosphogenesis of delicate specimens.

Smear slides from the lower transitional unit and the green marlstone contain clusters of microglobular apatite that resemble spherulites grown in gels in the laboratory (supporting information Figure S14; Pl. 1, 7–9),

and microbial Paleoproterozoic phosphorite (Hiatt et al., 2015). A range of other apatite forms are observed, which also could be of biological origin but whose affinity is also unclear (supporting information Figure S9; Pl. 17, 21, 22; supporting information Figure S14; Pl. 2–6). Epifluorescence images also show the blades of apatite focused between 616.58–616.56 mbsf (Figure 3; Pl. 4) as well as occurring in elongated lenses between 616.6–616.57 mbsf. These lenses contain rare grains of apatite (supporting information Figure S12; Pl. 12) and appear to be organic-rich based on their appearance in cross-polarized light (Figure 3; Pl. 3). We speculate that these grains originate from microbial mats that thrived during the time interval represented by the boundary between the transitional unit and the green marlstone. Such mats may have occupied the shallow water regions near the crater rim and these grains may have been transported by the intense storms expected with the climatic changes across the K-Pg event (Covey et al., 1994; Emanuel et al., 1995).

The occurrence of microbial mats at the time of the upper transitional unit and in the green marlstone has already been proposed based on elevated 3β-methylhopane indices in samples between 616.62 and 616.55 mbsf (Schaefer et al., 2020) which signify methanotrophic bacteria. Schaefer et al. (2020) postulated that the microbial compounds were redeposited from shallower parts of the crater. Today phosphatized microbial mats accumulate in upwelling settings along continental margins where the flux of organic carbon results in pore water supersaturation and subsequent precipitation of apatite following bacterial phosphate remineralization (Crosby & Bailey, 2012). Phosphate is generally rare in sediments deposited in deeper ocean regions. Elevated P levels may be a response to eutrophication that followed the decimation of planktic producers at the K-Pg boundary (Zachos et al., 1989); indeed apatite fossils are also found in samples from the Fish Clay at Stevns Klint (supporting information Figure S14; Pl. 10–12) that are thought to date to centuries and millennia after the impact. Resurge into the crater via the ~2 km deep northeast ramp to the Gulf of Mexico (Gulick et al., 2008) (Figure 10) could have delivered nutrient-rich waters but microbial activity would have readily depleted nutrient levels; thus there is likely another source of P. Occurrence of apatite in chlorite veins lower in the transitional unit (Figure 9; Pl. 7) suggests a connection between hydrothermal activity and P supply; indeed P is often enriched in late stage pegmatite fluids (Bucher & Stober, 2010). Thus the nascent crater may have provided a productive refuge for survivors, including the planktic foraminifera, explaining their earlier recovery.

Evidence for diverse life including morphological and molecular fossils(Lowery et al., 2018) (Bralower et al., 2020; Schaefer et al., 2020) from Chicxulub suggests that the crater became rapidly habitable in the immediate aftermath of the impact (Figure 11), possibly earlier than in other parts of the ocean. This suggests that the unique crater environment allowed life to flourish. We speculate that heat and nutrients from the hydrothermal system were instrumental in sustaining a diverse community of primitive life, and this community likely played a role in survival of higher orders of organisms, including pelagic crustaceans and fish (Sibert et al., 2014). The rapid appearance of life in the early Chicxulub crater, including organisms at a range of trophic levels, demonstrates the resiliency of life under extraordinarily harsh conditions, which has important ramifications for early life on Earth and life on other planets (Russell & Hall, 2006).

4. Conclusions

An expanded record from the peak ring of the Chicxulub crater illustrates the connection between environment and recovery of life in the nascent Chicxulub crater. Water temperatures in the were in excess of 70°C immediately after the K-Pg impact with heat derived from the central melt sheet. The cooler peak ring location was habitable within days to years of the impact with survivor nannoplankton and monospecific, red-tide dinocyst assemblage arriving in the aftermath of the tsunami waves. A monogeneric calcareous dinoflagellate resting cyst assemblage is found at levels where charcoal and the Ir anomaly indicate atmospheric fallout, and a possible interpretation is that the absence of photosynthetic plankton was a response to low light levels. Microbial fossils are found throughout the sequence suggesting a thriving bacterial community potentially supported by nutrients from hydrothermal activity. This productivity likely supported the recovery of organisms representing a range of trophic levels including planktic foraminifera, pelagic crustaceans and fishes over an interval of years to no more than a few millennia.

Conflict of Interest

The authors declare no conflicts of interest relevant to this study.

Data Availability Statement

The data that support the findings of this study are available in the PANGAEA database (https://www.pangaea.de/). This research used samples and data provided by IODP.

References

Abramov, O., & Kring, D. A. (2007). Numerical modeling of impact-induced hydrothermal activity at the Chicxulub crater. *Meteoritics and Planetary Science*, *42*, 93–112. https://doi.org/10.1111/j.1945-5100.2007.tb00220.x

Agrinier, P., Deutsch, A., Schärer, U., & Martinez, I. (2001). Fast back-reactions of shock-released CO_2 from carbonates: An experimental approach. *Geochimica et Cosmochimica Acta*, *65*, 2615–2632. https://doi.org/10.1016/s0016-7037(01)00617-2

Akahane, H., Furuno, T., Miyajima, H., Yoshikawa, T., & Yamamoto, S. (2004). Rapid wood silicification in hot spring water: An explanation of silicification of wood during the Earth's history. *Sedimentary Geology*, *169*, 219–228. https://doi.org/10.1016/j.sedgeo.2004.06.003

Al-Bassam, K., & Halodová, P. (2018). Fossil bacteria in Cenomanian–Turonian phosphate nodules and coprolites, Bohemian Cretaceous Basin, Czech Republic. *Annales societatis geologorum poloniae* (Vol. 88, pp. 257–272). Kraków, Poland. https://doi.org/10.14241/asgp.2018.009

Alegret, L., & Thomas, E. (2001). Upper Cretaceous and lower Paleogene benthic foraminifera from northeastern Mexico. *Micropaleontology*, *47*, 269–316. https://doi.org/10.2113/47.4.269

Alfaro, M. E., Faircloth, B. C., Harrington, R. C., Sorenson, L., Friedman, M., Thacker, C. E., et al. (2018). Explosive diversification of marine fishes at the Cretaceous–Palaeogene boundary. *Nature Ecology & Evolution*, *2*, 688. https://doi.org/10.1038/s41559-018-0494-6

Alvarez, L. W., Alvarez, W., Asaro, F., & Michel, H. V. (1980). Extraterrestrial cause for the Cretaceous-Tertiary extinction. *Science*, *208*, 1095–1108. https://doi.org/10.1126/science.208.4448.1095

Artemieva, N., & Morgan, J. (2009). Modeling the formation of the K–Pg boundary layer. *Icarus*, *201*, 768–780. https://doi.org/10.1016/j.icarus.2009.01.021

Artemieva, N., & Morgan, J. (2017). Quantifying the release of climate-active gases by large meteorite impacts with a case study of Chicxulub. *Geophysical Research Letters*, *44*, 11,0180–11,0188. https://doi.org/10.1002/2017GL074879

Artemieva, N., & Morgan, J. (2020). Global K-Pg layer deposited from a dust cloud. *Geophysical Research Letters*, *47*, e2019GL086562. https://doi.org/10.1029/2019GL086562

Arz, J. A., Alegret, L., & Arenillas, I. (2004). Foraminiferal biostratigraphy and paleoenvironmental reconstruction at the Yaxcopoil-1 drill hole, Chicxulub crater, Yucatán Peninsula. *Meteoritics & Planetary Science*, *39*, 1099–1111. https://doi.org/10.1111/j.1945-5100.2004.tb01131.x

Astrop, T. I., Sahni, V., Blackledge, T. A., & Stark, A. Y. (2015). Mechanical properties of the chitin-calcium-phosphate "clam shrimp" carapace (Branchiopoda: Spinicaudata): Implications for taphonomy and fossilization. *Journal of Crustacean Biology*, *35*, 123–131. https://doi.org/10.1163/1937240x-00002332

Atkins, A., Dean, M. N., Habegger, M. L., Motta, P. J., Ofer, L., Repp, F., et al. (2014). Remodeling in bone without osteocytes: Billfish challenge bone structure–function paradigms. *Proceedings of the National Academy of Sciences*, *111*, 16,047–16,052. https://doi.org/10.1073/pnas.1412372111

Beck, W. C., Grossman, E. L., & Morse, J. W. (2005). Experimental studies of oxygen isotope fractionation in the carbonic acid system at 15°, 25°, and 40°C. *Geochimica et Cosmochimica Acta*, *69*, 3493–3503. https://doi.org/10.1016/j.gca.2005.02.003

Belza, J., Goderis, S., Keppens, E., Vanhaecke, F., & Claeys, P. (2012). An emplacement mechanism for the mega-block zone within the Chicxulub crater, (Yucatán, Mexico) based on chemostratigraphy. *Meteoritics & Planetary Science*, *47*, 400–413. https://doi.org/10.1111/j.1945-5100.2012.01345.x

Berggren, W. A., Kent, D. V., Swisher, C. C. III, & Aubry, M.-P. (1995). A revised Cenozoic geochronology and chronostratigraphy. In *Geochronology, Time Scales and Global Stratigraphic Correlation*, *SEPM Special Publication No. 54* (pp. 129–212). Tulsa, OK.

Birch, H. S., Coxall, H. K., & Pearson, P. N. (2012). Evolutionary ecology of Early Paleocene planktonic foraminifera: Size, depth habitat and symbiosis. *Paleobiology*, *38*, 374–390. https://doi.org/10.1666/11027.1

Bralower, T. J., Cosmidis, J., Heaney, P., Kump, L. R., Morgan, J., Harper, D., et al. (2020). Origin of a global carbonate layer deposited in the aftermath of the Cretaceous-Paleogene boundary impact. *Earth and Planetary Science Letters*, *548*, 116476. https://doi.org/10.1016/j.epsl.2020.116476

Brenner, D. C., Passey, B. H., & Stolper, D. A. (2018). Influence of water on clumped-isotope bond reordering kinetics in calcite. *Geochimica et Cosmochimica Acta*, *224*, 42–63. https://doi.org/10.1016/j.gca.2017.12.026

Brinkhuis, H., Bujak, J., Smit, J., Versteegh, G., & Visscher, H. (1998). Dinoflagellate-based sea surface temperature reconstructions across the Cretaceous–Tertiary boundary. *Paleogeography, Palaeoclimatology, Palaeoecology*, *141*, 67–83. https://doi.org/10.1016/s0031-0182(98)00004-2

Brinkhuis, H., & Zachariasse, W. J. (1988). Dinoflagellate cysts, sea level changes and planktonic foraminifers across the Cretaceous-Tertiary boundary at El Haria, northwest Tunisia. *Marine Micropaleontology*, *13*, 153–191. https://doi.org/10.1016/0377-8398(88)90002-3

Brugger, J., Feulner, G., & Petri, S. (2017). Baby, it's cold outside: Climate model simulations of the effects of the asteroid impact at the end of the Cretaceous. *Geophysical Research Letters*, *44*, 419–427. https://doi.org/10.1002/2016GL072241

Bucher, K., & Stober, I. (2010). Fluids in the upper continental crust. *Geofluids*, *10*, 241–253. https://doi.org/10.1002/9781444394900.ch17

Chandran, R., Williams, L., Hung, A., Nowlin, K., & LaJeunesse, D. (2016). SEM characterization of anatomical variation in chitin organization in insect and arthropod cuticles. *Micron*, *82*, 74–85. https://doi.org/10.1016/j.micron.2015.12.010

Charlier, B., Tissot, F., Dauphas, N., & Wilson, C. (2019). Nucleosynthetic, radiogenic and stable strontium isotopic variations in fine-and coarse-grained refractory inclusions from Allende. *Geochimica et Cosmochimica Acta*, *265*, 413–430. https://doi.org/10.1016/j.gca.2019.09.005

Chiarenza, A. A., Farnsworth, A., Mannion, P. D., Lunt, D. J., Valdez, P. J., Morgan, J. V., & Allison, P. A. (2020). Asteroid impact, not volcanism, caused the end-Cretaceous dinosaur extinction. *Proceedings of the National Academy of Sciences of the United States of America*, *117*. https://doi.org/10.1073/pnas.2006087117

Cockell, C. S., Coolen, M. J., Grice, K., & Schaefer, B. (2019). 316-3. Microbial communities and impact enhanced habitats in the Chicxulub impact crater. In *Astrobiology science conference*. Washington, DC: AGU.

Cockell, C. S., Osinski, G. R., & Lee, P. (2003). The impact crater as a habitat: Effects of impact processing of target materials. *Astrobiology*, *3*, 181–191. https://doi.org/10.1089/153110703321632507

Cohen, L., Dean, M., Shipov, A., Atkins, A., Monsonego-Ornan, E., & Shahar, R. (2012). Comparison of structural, architectural and mechanical aspects of cellular and acellular bone in two teleost fish. *Journal of Experimental Biology*, *215*, 1983–1993. https://doi.org/10.1242/jeb.064790

Collettini, C., Viti, C., Tesei, T., & Mollo, S. (2013). Thermal decomposition along natural carbonate faults during earthquakes. *Geology*, *41*, 927–930. https://doi.org/10.1130/g34421.1

Colodner, D. C., Boyle, E. A., Edmond, J. M., & Thomson, J. (1992). Post-depositional mobility of platinum, iridium and rhenium in marine sediments. *Nature*, *358*, 402. https://doi.org/10.1038/358402a0

Cosmidis, J., Benzerara, K., Gheerbrant, E., Estève, I., Bouya, B., & Amaghzaz, M. (2013). Nanometer-scale characterization of exceptionally preserved bacterial fossils in Paleocene phosphorites from Ouled A bdoun (Morocco). *Geobiology*, *11*, 139–153. https://doi.org/10.1111/gbi.12022

Cosmidis, J., Benzerara, K., Menguy, N., & Arning, E. (2013). Microscopy evidence of bacterial microfossils in phosphorite crusts of the Peruvian shelf: Implications for phosphogenesis mechanisms. *Chemical Geology*, *359*, 10–22. https://doi.org/10.1016/j.chemgeo.2013.09.009

Covey, C., Thompson, S. L., Weissman, P. R., & MacCracken, M. C. (1994). Global climatic effects of atmospheric dust from an asteroid or comet impact on Earth. *Global and Planetary Change*, *9*, 263–273. https://doi.org/10.1016/0921-8181(94)90020-5

Coxall, H. K., D'Hondt, S., & Zachos, J. C. (2006). Pelagic evolution and environmental recovery after the Cretaceous-Paleogene mass extinction. *Geology*, *34*. https://doi.org/10.1130/g21702.1

Crosby, C. H., & Bailey, J. (2012). The role of microbes in the formation of modern and ancient phosphatic mineral deposits. *Frontiers in Microbiology*, *3*, 241. https://doi.org/10.3389/fmicb.2012.00241

DePalma, R. A., Smit, J., Burnham, D. A., Kuiper, K., Manning, P. L., Oleinik, A., et al. (2019). A seismically induced onshore surge deposit at the KPg boundary, North Dakota. *Proceedings of the National Academy of Sciences*, *116*, 8190–8199. https://doi.org/10.1073/pnas.1817407116

Dickin, A. P. (2018). *Radiogenic isotope geology*. Cambridge, UK: Cambridge University Press.

Durand-Manterola, H. J. & Cordero-Tercero, G. Assessments of the energy, mass and size of the Chicxulub impactor. *arXiv preprint arXiv:1403.6391* (2014).

Eiler, J. M. (2007). Clumped-isotope geochemistry—The study of naturally-occurring, multiply-substituted isotopologues. *Earth and Planetary Science Letters*, *262*, 309–327. https://doi.org/10.1016/j.epsl.2007.08.020

Emanuel, K. A., Speer, K., Rotunno, R., Srivastava, R., & Molina, M. (1995). Hypercanes: A possible link in global extinction scenarios. *Journal of Geophysical Research*, *100*, 13,755–13,765. https://doi.org/10.1029/95JD01368

Emslie, S. D., Brasso, R., Patterson, W. P., Valera, A. C., McKenzie, A., Silva, A. M., et al. (2015). Chronic mercury exposure in Late Neolithic/Chalcolithic populations in Portugal from the cultural use of cinnabar. *Scientific Reports*, *5*, 14679. https://doi.org/10.1038/srep14679

Farley, K., & Eltgroth, S. (2003). An alternative age model for the Paleocene–Eocene thermal maximum using extraterrestrial ³He. *Earth and Planetary Science Letters*, *208*, 135–148. https://doi.org/10.1016/s0012-821x(03)00017-7

Faure, G., & Powell, J. L. (1972). *Strontium isotope geology* (pp. 78–91). Berlin, Heidelberg, New York: Springer.

Ferry, J. M., Passey, B. H., Vasconcelos, C., & Eiler, J. M. (2011). Formation of dolomite at 40–80 ° C in the Latemar carbonate buildup, Dolomites, Italy, from clumped isotope thermometry. *Geology*, *39*, 571–574. https://doi.org/10.1130/g31845.1

Forchhammer, G. (1825). *Om de geognostiske forhold i en deel af Sjelland og naboøerne*.

Friedman, M. (2009). Ecomorphological selectivity among marine teleost fishes during the end-Cretaceous extinction. *Proceedings of the National Academy of Sciences*, *106*, 5218–5223. https://doi.org/10.1073/pnas.0808468106

Gabitov, R. I., Watson, E. B., & Sadekov, A. (2012). Oxygen isotope fractionation between calcite and fluid as a function of growth rate and temperature: An in situ study. *Chemical Geology*, *306*, 92–102. https://doi.org/10.1016/j.chemgeo.2012.02.021

Ghosh, P., Adkins, J., Affek, H., Balta, B., Guo, W., Schauble, E. A., et al. (2006). 13C–18O bonds in carbonate minerals: A new kind of paleothermometer. *Geochimica et Cosmochimica Acta*, *70*, 1439–1456. https://doi.org/10.1016/j.gca.2005.11.014

Goderis, S., Sato, H., Ferrière, L., Schmitz, B., Burney, D., Bralower, T. J., et al. (2019). The final settling of meteoritic matter on the peak-ring of the Chicxulub impact structure ar Site M0077A of IODP-ICDP expedition 364. In *Large meteorite impacts and planetary evolution VI, Abstract #5068*. Houston, TX: Lunar and Planetary Institute.

Goto, K., Tada, R., Tajika, E., Bralower, T. J., Hasegawa, T., & Matsui, T. (2004). Evidence for ocean water invasion into the Chicxulub crater at the Cretaceous/Tertiary boundary. *Meteoritics & Planetary Science*, *39*, 1233–1247. https://doi.org/10.1111/j.1945-5100.2004.tb01139.x

Gulick, S. P., Barton, P. J., Christeson, G. L., Morgan, J. V., McDonald, M., Mendoza-Cervantes, K., et al. (2008). Importance of pre-impact crustal structure for the asymmetry of the Chicxulub impact crater. *Nature Geoscience*, *1*, 131–135. https://doi.org/10.1038/ngeo103

Gulick, S., Morgan, J., Mellett, C. L., & the Expedition 364 Scientists (2017). *Expedition 364 preliminary report: Chicxulub: Drilling the K-Pg impact crater*. College Station, TX: International Ocean Drilling Program.

Gulick, S., Bralower, T. J., Ormö, J., Hall, B., Grice, K., Schaefer, B., et al. (2019). The first day of the Cenozoic. *PNAS*, *113*, 19,342–19,351. https://doi.org/10.1073/pnas.1909479116

Gulick, S., Christeson, G. L., Barton, P. J., Grieve, R. A. F., Morgan, J. V., & Urrutia-Fucugauchi, J. (2013). Geophysical characterization of the Chicxulub impact crater. *Reviews of Geophysics*, *51*, 31–52. https://doi.org/10.1002/rog.20007

Hamann, C., Bläsing, S., Hecht, L., Schäffer, S., Deutsch, A., Osterholz, J., & Lexow, B. (2018). The reaction of carbonates in contact with laser-generated, superheated silicate melts: Constraining impact metamorphism of carbonate-bearing target rocks. *Meteoritics & Planetary Science*, *53*, 1644–1686. https://doi.org/10.1111/maps.13133

He, S., & Morse, J. W. (1993). The carbonic acid system and calcite solubility in aqueous Na-K-Ca-Mg-Cl-SO4 solutions from 0° to 90°C. *Geochimica et Cosmochimica Acta*, *57*, 3533–3554. https://doi.org/10.1016/0016-7037(93)90137-l

Hecht, L., Wittmann, A., Schmitt, R.-T., & Stöffler, D. (2004). Composition of impact melt particles and the effects of post-impact alteration in suevitic rocks at the Yaxcopoil-1 drill core, Chicxulub crater, Mexico. *Meteoritics and Planetary Science*, *39*, 1169–1186. https://doi.org/10.1111/j.1945-5100.2004.tb01135.x

Henkes, G. A., Passey, B. H., Grossman, E. L., Shenton, B. J., Pérez-Huerta, A., & Yancey, T. E. (2014). Temperature limits for preservation of primary calcite clumped isotope paleotemperatures. *Geochimica et Cosmochimica Acta*, *139*, 362–382. https://doi.org/10.1016/j.gca.2014.04.040

Hiatt, E. E., Pufahl, P. K., & Edwards, C. T. (2015). Sedimentary phosphate and associated fossil bacteria in a Paleoproterozoic tidal flat in the 1.85 Ga Michigamme Formation, Michigan, USA. *Sedimentary Geology*, *319*, 24–39. https://doi.org/10.1016/j.sedgeo.2015.01.006

Hildebrand, A. R., Penfield, G. T., Kring, D. A., Pilkington, M., Antonio Camargo, Z., Jacobsen, S. B., & Boynton, W. V. (1991). Chicxulub crater: A possible Cretaceous/Tertiary boundary impact crater on the Yucatan Peninsula, Mexico. *Geology*, *19*, 867–871. https://doi.org/10.1130/0091-7613(1991)019<0867:ccapct>2.3.co;2

Hollund, H. I., Blank, M., & Sjögren, K.-G. (2018). Dead and buried? Variation in post-mortem histories revealed through histotaphonomic characterisation of human bone from megalithic graves in Sweden. *PLoS ONE*, *13*, e0204662. https://doi.org/10.1371/journal.pone.0204662

Horton, J. M., & Summers, A. P. (2009). The material properties of acellular bone in a teleost fish. *Journal of Experimental Biology*, *212*, 1413–1420. https://doi.org/10.1242/jeb.020636

Hull, P. M., Bornemann, A., Penman, D. E., Henehan, M. J., Norris, R. D., Wilson, P. A., et al. (2020). On impact and volcanism across the Cretaceous-Paleogene boundary. *Science*, *367*, 266–272. https://doi.org/10.1126/science.aay5055

Hull, P. M., Norris, R. D., Bralower, T. J., & Schueth, J. D. (2011). A role for chance in marine recovery from the end-Cretaceous extinction. *Nature Geoscience*, *4*, 856–860. https://doi.org/10.1038/ngeo1302

Jiang, S., Bralower, T. J., Patzkowsky, M. E., Kump, L. R., & Schueth, J. D. (2010). Geographic controls on nannoplankton extinction across the Cretaceous/Palaeogene boundary. *Nature Geoscience*, *3*, 280–285. https://doi.org/10.1038/ngeo775

Jones, B. (2017). Review of aragonite and calcite crystal morphogenesis in thermal spring systems. *Sedimentary Geology*, *354*, 9–23. https://doi.org/10.1016/j.sedgeo.2017.03.012

Jones, H. L., Lowery, C. M., & Bralower, T. J. (2019). Calcareous nannoplankton "boom-bust" successions in the Cretaceous-Paleogene (K-Pg) impact crater suggests ecological experimentation at "ground zero". *Geology*, *47*, 753–756. https://doi.org/10.1130/g46143.1

Jones, T. P., & Lim, B. (2000). Extraterrestrial impacts and wildfires. *Paleogeography, Palaeoclimatology, Palaeoecology*, *164*, 57–66. https://doi.org/10.1016/s0031-0182(00)00175-9

Kaiho, K., Oshima, N., Adachi, K., Adachi, Y., Mizukami, T., Fujibayashi, M., & Saito, R. (2016). Global climate change driven by soot at the K-Pg boundary as the cause of the mass extinction. *Scientific Reports*, *6*, 28427. https://doi.org/10.1038/srep28427

Kim, S.-T., & O'Neil, J. R. (1997). Equilibrium and nonequilibrium oxygen isotope effects in synthetic carbonates. *Geochimica et Cosmochimica Acta*, *61*, 3461–3475. https://doi.org/10.1016/s0016-7037(97)00169-5

Kring, D. (2007). A. The Chicxulub impact event and its environmental consequences at the Cretaceous–Tertiary boundary. *Paleogeography, Palaeoclimatology Palaeoecology*, *255*, 4–21. https://doi.org/10.1016/j.palaeo.2007.02.037

Kring, D. A. (1995). The dimensions of the Chicxulub impact crater and impact melt sheet. *Journal of Geophysical Research: Planets*, *100*, 16,979–16,986. https://doi.org/10.1029/95JE01768

Kring, D. A. (2005). Hypervelocity collisions into continental crust composed of sediments and an underlying crystalline basement: Comparing the Ries (~24 km) and Chicxulub (~180 km) impact craters. *Chemie der Erde-Geochemistry*, *65*, 1–46. https://doi.org/10.1016/j.chemer.2004.10.003

Kring, D. A., & Boynton, W. V. (1992). Petrogenesis of an augite-bearing melt rock in the Chicxulub structure and its relationship to K/T impact spherules in Haiti. *Nature*, *358*, 141. https://doi.org/10.1038/358141a0

Kring, D. A., Tikoo, S. M., Schmieder, M., Riller, U., Rebolledo-Vieyra, M., Simpson, S. L., et al. (2020). Probing the hydrothermal system of the Chicxulub Crater. *Science Advances*, *6*. https://doi.org/10.1126/sciadv.aaz3053

Kruge, M. A., Stankiewicz, B. A., Crelling, J. C., Montanari, A., & Bensley, D. F. (1994). Fossil charcoal in Cretaceous-Tertiary boundary strata: Evidence for catastrophic firestorm and megawave. *Geochimica et Cosmochimica Acta*, *58*, 1393–1397. https://doi.org/10.1016/0016-7037(94)90394-8

Lammers, L. N., & Mitnick, E. H. (2019). Magnesian calcite solid solution thermodynamics inferred from authigenic deep-sea carbonate. *Geochimica et Cosmochimica Acta*, *248*, 343–355. https://doi.org/10.1016/j.gca.2019.01.006

Lowery, C. M., Bralower, T. J., Owens, J. D., Rodríguez-Tovar, F. J., Jones, H., Smit, J., et al. (2018). Rapid recovery of life at ground zero of the end-Cretaceous mass extinction. *Nature*, *558*, 288–291. https://doi.org/10.1038/s41586-018-0163-6

Lüders, V., & Rickers, K. (2004). Fluid inclusion evidence for impact-related hydrothermal fluid and hydrocarbon migration in Creataceous sediments of the ICDP-Chicxulub drill core Yax-1. *Meteoritics and Planetary Science*, *39*, 1187–1197. https://doi.org/10.1111/j.1945-5100.2004.tb01136.x

Lyons, S. L., Karp, A. T., Bralower, T. J., Grice, K., Schaefer, B., Gulick, S. P. S., et al. (2020). Organic matter from the Chicxulub crater exacerbated the K–Pg impact winter. *PNAS*. https://doi.org/10.1073/pnas.2004596117

MacLeod, K. G., Huber, B. T., & Fullagar, P. D. (2001). Evidence for a small (~0.000030) but resolvable increase in seawater $^{87}Sr/^{86}Sr$ ratios across the Cretaceous-Tertiary boundary. *Geology*, *29*, 303–306. https://doi.org/10.1130/0091-7613(2001)029<0303:efasbr>2.0.co;2

Maggi, F. (2013). The settling velocity of mineral, biomineral, and biological particles and aggregates in water. *Journal of Geophysical Research: Oceans*, *118*, 2118–2132. https://doi.org/10.1002/jgrc.20086

Martin, E., & Macdougall, J. (1991). Seawater Sr isotopes at the Cretaceous/Tertiary boundary. *Earth and Planetary Science Letters*, *104*, 166–180. https://doi.org/10.1016/0012-821x(91)90202-s

McArthur, J. & Howarth, R. (2004). Cambridge University Press: Cambridge, UK.

Melosh, H. J., Schneider, N., Zahnle, K. J., & Latham, D. (1990). Ignition of global wildfires at the Cretaceous/Tertiary boundary. *Nature*, *343*, 251. https://doi.org/10.1038/343251a0

Miller, M. F., Franchi, I. A., Thiemens, M. H., Jackson, T. L., Brack, A., Kurat, G., & Pillinger, C. T. (2002). Mass-independent fractionation of oxygen isotopes during thermal decomposition of carbonates. *Proceedings of the National Academy of Sciences*, *99*, 10,988–10,993. https://doi.org/10.1073/pnas.172378499

Morgan, J., & Gulick, S. (2018). Drilling the K-Pg impact crater: IODP-ICDP Expedition 364 results. In *LPI Contributions 2067*. Houston, TX: Lunar and Planetary Institute.

Morgan, J. V., & Warner, M. (1999). Chicxulub: The third dimension of a multi-ring impact basin. *Geology*, *27*, 407–410. https://doi.org/10.1130/0091-7613(1999)027<0407:cttdoa>2.3.co;2

Morgan, J. V., Gulick, S. P. S., Bralower, T., Chenot, E., Christeson, G., Claeys, P., et al. (2016). The formation of peak rings in large impact craters. *Science*, *354*, 878–882. https://doi.org/10.1126/science.aah6561

Mucci, A. (1983). The solubility of calcite and aragonite in seawater at various salinities, temperatures, and one atmosphere total pressure. *American Journal of Science*, *283*, 780–799. https://doi.org/10.2475/ajs.283.7.780

Newsom, H. E., Hagerty, J. J., & Thorsos, I. E. (2001). Location and sampling of aqueous and hydrothermal deposits in Martian impact craters. *Astrobiology*, *1*, 71–88. https://doi.org/10.1089/153110701750137459

Novellino, R., Prosser, G., Spiess, R., Viti, C., Agosta, F., Tavarnelli, E., & Bucci, F. (2015). Dynamic weakening along incipient low-angle normal faults in pelagic limestones (Southern Apennines, Italy). *Journal of the Geological Society*, *172*, 283–286. https://doi.org/10.1144/jgs2014-091

O'Sullivan, E. M., Goodhue, R., Ames, D. E., & Kamber, B. S. (2016). Chemostratigraphy of the Sudbury impact basin fill: Volatile metal loss and post-impact evolution of a submarine impact basin. *Geochimica et Cosmochimica Acta*, *183*, 198–233. https://doi.org/10.1016/j.gca.2016.04.007

Osinski, G. R., Tornabene, L. L., Banerjee, N. R., Cockell, C. S., Flemming, R., Izawa, M. R. M., et al. (2013). Impact-generated hydrothermal systems on Earth and Mars. *Icarus*, *224*, 347–363. https://doi.org/10.1016/j.icarus.2012.08.030

Pesquero, M. D., Souza-Egipsy, V., Alcalá, L., Ascaso, C., & Fernández-Jalvo, Y. (2013). Calcium phosphate preservation of faecal bacterial negative moulds in hyaena coprolites. *Acta Palaeontologica Polonica*, *59*, 997–1006. https://doi.org/10.4202/app.2012.0067

Petersen, S., Defliese, W. F., Saenger, C., Daëron, M., Huntington, K. W., John, C. M., et al. (2019). Effects of improved ^{17}O correction on inter-laboratory agreement in clumped isotope calibrations, estimates of mineral-specific offsets, and temperature dependence of acid digestion fractionation. *Geochemistry, Geophysics, Geosystems*, *20*, 3495–3519. https://doi.org/10.1029/2018GC008127

Pineda, A., Saladié, P., Expósito, I., Rodríguez-Hidalgo, A., Cáceres, I., Huguet, R., et al. (2017). Characterizing hyena coprolites from two latrines of the Iberian Peninsula during the Early Pleistocene: Gran Dolina (Sierra de Atapuerca, Burgos) and la Mina (Barranc de la Boella, Tarragona). *Palaeogeography, Palaeoclimatology, Palaeoecology*, *480*, 1–17. https://doi.org/10.1016/j.palaeo.2017.04.021

Plummer, L. N., & Busenberg, E. (1982). The solubilities of calcite, aragonite and vaterite in CO_2-H_2O solutions between 0° and 90°C, and an evaluation of the aqueous model for the system $CaCO_3$-CO_2-H_2O. *Geochimica et Cosmochimica Acta*, *46*, 1011–1040. https://doi.org/10.1016/0016-7037(82)90056-4

Pospichal, J. J., & Wise, S. W. Jr. (1990). Calcareous nannofossils across the K/T boundary, ODP hole 690C, Maud Rise, Weddell Sea. *Proceeding of the Ocean Drilling Program, Scientific Results*, *113*, 515–532. https://doi.org/10.2973/odp.proc.sr.113.204.1990

Prinn, R. G., & Fegley, B. Jr. (1987). Bolide impacts, acid rain, and biospheric traumas at the Cretaceous-Tertiary boundary. *Earth and Planetary Science Letters*, *83*, 1–15. https://doi.org/10.1016/0012-821x(87)90046-x

Ramírez-Reinat, E., & Garcia-Pichel, F. (2012). Prevalence of Ca2 + -ATPase-mediated carbonate dissolution among cyanobacterial euendoliths. *Applied and Environmental Microbiology*, *78*, 7–13. https://doi.org/10.1128/aem.06633-11

Rathbun, J. A., & Squyres, S. W. (2002). Hydrothermal systems associated with Martian impact craters. *Icarus*, *157*, 362–372. https://doi.org/10.1006/icar.2002.6838

Rodriguez-Navarro, C., Ruiz-Agudo, E., Luque, A., Rodriguez-Navarro, A. B., & Ortega-Huertas, M. (2009). Thermal decomposition of calcite: Mechanisms of formation and textural evolution of CaO nanocrystals. *American Mineralogist*, *94*, 578–593. https://doi.org/10.2138/am.2009.3021

Rodríguez-Tovar, F. J., Lowery, C., Bralower, T. J., Gulick, S., & Jones, H. (2020). Rapid macrobenthic diversification and stabilization after the end-Cretaceous mass extinction event. *Geology*. https://doi.org/10.1130/G47589.1

Rowe, A., Wilkinson, J., Coles, B., & Morgan, J. (2004). Chicxulub: Testing for post-impact hydrothermal input into the Tertiary ocean. *Journal Planetary Science Meteoritics*, *39*, 1223–1231. https://doi.org/10.1111/j.1945-5100.2004.tb01138.x

Russell, M. J., & Hall, A. J. (2006). The onset and early evolution of life. In *Memoirs-Geological Society of America* (Vol. 198, pp. 1–32). Boulder, CO: Geological Society of America. https://doi.org/10.1130/2006.1198(01)

Schaefer, B., Grice, K., Coolen, M. J. L., Summons, R. E., Cui, X., Bauersachs, T., et al. (2020). Microbial life in the nascent Chicxulub crater. *Geology*. https://doi.org/10.1130/G46799.1

Schmitt, R. T., Wittmann, A., & Stöffler, D. (2004). Geochemistry of drill core samples from Yaxcopoil-1, Chicxulub impact crater, Mexico. *Meteoritics & Planetary Science*, *39*, 979–1001. https://doi.org/10.1111/j.1945-5100.2004.tb00940.x

Schoene, B., Eddy, M. P., Samperton, K. M., Keller, C. B., Keller, G., Adatte, T., & Khadri, S. F. R. (2019). U-Pb constraints on pulsed eruption of the Deccan Traps across the end-Cretaceous extinction. *Science*, *363*, 862–866. https://doi.org/10.1126/science.aau2422

Schulte, P., Deutsch, A., Salge, T., Berndt, J., Kontny, A., MacLeod, K. G., et al. (2009). A dual-layer Chicxulub ejecta sequence with shocked carbonates from the Cretaceous–Paleogene (K–Pg) boundary, Demerara Rise, western Atlantic. *Geochimica et Cosmochimica Acta*, *73*, 1180–1204. https://doi.org/10.1016/j.gca.2008.11.011

Schulte, P., Alegret, L., Arenillas, I., Arz, J. A., Barton, P. J., Bown, P. R., et al. (2010). The Chicxulub asteroid impact and mass extinction at the Cretaceous-Paleogene boundary. *Science*, *327*, 1214–1218. https://doi.org/10.1126/science.1177265

Seidel, R., Lyons, K., Blumer, M., Zaslansky, P., Fratzl, P., Weaver, J. C., & Dean, M. N. (2016). Ultrastructural and developmental features of the tessellated endoskeleton of elasmobranchs (sharks and rays). *Journal of Anatomy*, *229*, 681–702. https://doi.org/10.1111/joa.12508

Shenton, B. J., Grossman, E. L., Passey, B. H., Henkes, G. A., Becker, T. P., Laya, J. C., et al. (2015). Clumped isotope thermometry in deeply buried sedimentary carbonates: The effects of bond reordering and recrystallization. *GSA Bulletin*, *127*, 1036–1051. https://doi.org/10.1130/b31169.1

Sibert, E. C., Hull, P. M., & Norris, R. D. (2014). Resilience of Pacific pelagic fish across the Cretaceous/Palaeogene mass extinction. *Nature Geoscience*, *7*, 667. https://doi.org/10.1038/ngeo2227

Sibert, E. C., & Norris, R. D. (2015). New age of fishes initiated by the Cretaceous−Paleogene mass extinction. *Proceedings of the National Academy of Sciences*, *112*, 8537–8542. https://doi.org/10.1073/pnas.1504985112

Smit, J., & Romein, A. (1985). A sequence of events across the Cretaceous-Tertiary boundary. *Earth and Planetary Science Letters*, *74*, 155–170. https://doi.org/10.1016/0012-821x(85)90019-6

Sprain, C. J., Renne, P. R., Vanderkluysen, L., Pande, K., Self, S., & Mittal, T. (2019). The eruptive tempo of Deccan volcanism in relation to the Cretaceous-Paleogene boundary. *Science*, *363*, 866–870. https://doi.org/10.1126/science.aav1446

Stokes, G. G. (1850). On the effect of the internal friction of fluids on the motion of pendulums. *Transactions of the Cambridge Philosophical Society IX*, *reprinted in Mathematical and Physical Papers*, *3*, 1–86. https://doi.org/10.1017/CBO9780511702266

Tabor, C. R., Bardeen, C. G., Otto-Bliesner, B. L., Garcia, R. R., & Toon, O. B. (2020). Causes and climatic consequences of the impact winter at the Cretaceous-Paleogene boundary. *Geophysical Research Letters*, *47*, e60121. https://doi.org/10.1029/2019GL085572

Thompson, J. B. (2000). *Microbial sediments* (pp. 250–260). Berlin, Heidelberg: Springer.

Toon, O. B., Pollack, J. B., Ackerman, T. P., Turco, R. P., McKay, C. P., & Liu, M. S. (1982). Evolution of an impact-generated dust cloud and its effects on the atmosphere. In *Geological Society of America Special Papers* (pp. 187–200). Boulder, CO: Geological Society of America.

Tschudy, R., Pillmore, C., Orth, C., Gilmore, J., & Knight, J. (1984). Disruption of the terrestrial plant ecosystem at the Cretaceous-Tertiary boundary, Western Interior. *Science*, *225*, 1030–1032. https://doi.org/10.1126/science.225.4666.1030

Tuchscherer, M. G. (2008). *The petrology and geochemistry of the impactite sequence and selected target rocks from the Yaxcopoil-1 borehole*. Yucatan Peninsula, Mexico: Chicxulub Impact Structure.

Vellekoop, J., Sluijs, A., Smit, J., Schouten, S., Weijers, J. W. H., Damste, J. S. S., & Brinkhuis, H. (2014). Rapid short-term cooling following the Chicxulub impact at the Cretaceous–Paleogene boundary. *Proceedings of the National Academy of Sciences of the United States of America*, *111*, 7537–7541. https://doi.org/10.1073/pnas.1319253111

Vellekoop, J., Woelders, L., van Helmond, N. A. G. M., Galeotti, S., Smit, J., Slomp, C. P., et al. (2018). Shelf hypoxia in response to global warming after the Cretaceous-Paleogene boundary impact. *Geology*, *46*, 683–686. https://doi.org/10.1130/g45000.1

Wang, Y.-Y., Yao, Q.-Z., Zhou, G.-T., & Fu, S.-Q. (2013). Formation of elongated calcite mesocrystals and implication for biomineralization. *Chemical Geology*, *360*, 126–133. https://doi.org/10.1016/j.chemgeo.2013.10.013

Wasserburg, G., Papanastassiou, D., & Sanz, H. (1969). Initial strontium for a chondrite and the determination of a metamorphism or formation interval. *Earth and Planetary Science Letters*, *7*, 33–43. https://doi.org/10.1016/0012-821x(69)90008-9

Whalen, M. T., Gulick, S., Pearson, Z. F., & Norris, R. D. (2013). Annealing the Chicxulub impact: Paleogene Yucatán carbonate slope development in the Chicxulub impact basin, Mexico. In *Special Publication-SEPM* (Vol. 105, pp. 282–304). Tulsa, OK: Society for Sedimentary Geology.

Whalen, M. T., Gulick, S. P. S., Lowery, C., Bralower, T. J., Morgan, J. V., Grice, K., et al. (2018). Winding down the Chicxulub impact: The transition between impactites and normal marine sedimentation. In *American Geophysical Union Fall Meeting Abstracts, PP53B-08*.

Wolbach, W. S., Gilmour, I., & Anders, E. (1990). Major wildfires at the Cretaceous/Tertiary boundary. In *Geological society of America Special Paper* (Vol. 247, pp. 391–400). Boulder, CO: Geological Society of America.

Xiao, S., & Schiffbauer, J. D. (2009). *From fossils to astrobiology* (pp. 89–117). Dordrecht: Springer.

Yancey, T. E., & Guillemette, R. N. (2008). Carbonate accretionary lapilli in distal deposits of the Chicxulub impact event. *Geological Society of America Bulletin*, *120*, 1105–1118. https://doi.org/10.1130/b26146.1

Zachos, J. C., Arthur, M. A., & Dean, W. E. (1989). Geochemical evidence for suppression of pelagic marine productivity at the Cretaceous/Tertiary boundary. *Nature*, *337*, 61. https://doi.org/10.1038/337061a0

Zatoń, M., Niedźwiedzki, G., Marynowski, L., Benzerara, K., Pott, C., Cosmidis, J., et al. (2015). Coprolites of Late Triassic carnivorous vertebrates from Poland: An integrative approach. *Paleogeography, Palaeoclimatology, Palaeoecology*, *430*, 21–46. https://doi.org/10.1016/j.palaeo.2015.04.009

Zürcher, L., & Kring, D. A. (2004). Hydrothermal alteration in the core of the Yaxcopoil-1 borehole, Chicxulub impact structure, Mexico. *Meteoritics and Planetary Science*, *39*, 1199–1221. https://doi.org/10.1111/j.1945-5100.2004.tb01137.x

References From the Supporting Information

Luz, B., & Barkan, E. (2010). Variations of $^{17}O/^{16}O$ and $^{18}O/^{16}O$ in meteoric waters. *Geochimica et Cosmochimica Acta*, *74*, 6276–6286. https://doi.org/10.1016/j.gca.2010.08.016

Passey, B. H., Hu, H., Ji, H., Montanari, S., Li, S., Henkes, G. A., & Levin, N. E. (2014). Triple oxygen isotopes in biogenic and sedimentary carbonates. *Geochimica et Cosmochimica Acta*, *141*, 1–25. https://doi.org/10.1016/j.gca.2014.06.006